Spatially Resolved Chandra Spectroscopy of the Large Magellanic Cloud Supernova Remnant N132D

Piyush Sharda[1,2,3,4] , Terrance J. Gaetz[1] , Vinay L. Kashyap[1] , and Paul P. Plucinsky[1]
[1] Harvard-Smithsonian Center for Astrophysics, 60 Garden St., Cambridge, MA 02140, USA; piyush.sharda@anu.edu.au, tgaetz@cfa.harvard.edu
[2] Research School of Astronomy and Astrophysics, Australian National University, Canberra, ACT 2611, Australia
[3] Department of Physics, Birla Institute of Technology and Science, Pilani, Rajasthan 333031, India
[4] Australian Research Council Centre of Excellence for All Sky Astrophysics in 3 Dimensions (ASTRO 3D), Australia

Abstract

We perform detailed spectroscopy of the X-ray-brightest supernova remnant in the Large Magellanic Cloud (LMC), N132D, using Chandra archival observations. By analyzing the spectra of the entire well-defined rim, we determine the mean abundances for O, Ne, Mg, Si, S, and Fe for the local LMC environment. We find evidence of enhanced O on the northwestern and S on the northeastern blast wave. By analyzing spectra interior to the remnant, we confirm the presence of a Si-rich, relatively hot plasma ($\gtrsim 1.5\,\mathrm{keV}$) that is also responsible for the Fe K emission. Chandra images show that the Fe K emission is distributed throughout the interior of the southern half of the remnant but does not extend out to the blast wave. We estimate the progenitor mass to be $15 \pm 5\,M_\odot$ using abundance ratios in different regions that collectively cover a large fraction of the remnant, as well as from the radius of the forward shock compared with models of an explosion in a cavity created by stellar winds. We fit ionizing and recombining plasma models to the Fe K emission and find that the current data cannot distinguish between the two, so the origin of the high-temperature plasma remains uncertain. Our analysis is consistent with N132D being the result of a core-collapse supernova in a cavity created by its intermediate-mass progenitor.

Unified Astronomy Thesaurus concepts: Core-collapse supernovae (304); Interstellar medium (847); X-ray observatories (1819); X-ray astronomy (1810); Plasma astrophysics (1261); Shocks (2086); Interstellar abundances (832); Metallicity (1031); Large Magellanic Cloud (903); High resolution spectroscopy (2096)

1. Introduction

Magellanic cloud supernova remnant (MCSNR) J0525-6938 (commonly referred to as N132D, following the catalog by Henize 1956) is the X-ray-brightest SNR in the Large Magellanic Cloud (LMC; Long & Helfand 1979) with an X-ray luminosity of $L_X \sim 3 \times 10^{37}\,\mathrm{erg\,s^{-1}}$ (Maggi et al. 2016).[5] It was first classified as a core-collapse supernova (CCSN) by Westerlund & Mathewson (1966) and has been subsequently studied in great detail over the last few decades (e.g., Favata et al. 1997; Xiao & Chen 2008; Bamba et al. 2018). Based on optical observations, it has been classified as an oxygen-rich remnant (Danziger & Dennefeld 1976; Lasker 1978, 1980), thought to have exploded inside a low-density cavity in the interstellar medium (ISM; Hughes 1987). Sutherland & Dopita (1995) discuss the origin of this cavity, which might have formed by a wind bubble mechanism common to Wolf–Rayet stars (Dwarkadas 2007). It has been proposed by Blair et al. (2000) that this remnant might be the outcome of a Type Ib supernova (core collapse) and is believed to be roughly 2500 yr old (Morse et al. 1995; Hughes et al. 1998; Chen et al. 2003; Vogt & Dopita 2011; Law et al. 2020).

Several characteristics of this remnant make it a useful laboratory for studying SNRs interacting with molecular clouds. Analysis of Nuclear Spectroscopic Telescope Array (NuSTAR) and Suzaku observations of N132D by Bamba et al. (2018) reinforce the claim by Dickel & Milne (1995) that this remnant is in the transition stage from a young to a middle-aged remnant. The integrated radio luminosity of N132D at 1 GHz is 50% of Cas A, an SNR that is $\sim 5.5\times$ smaller in diameter than N132D

(Dickel & Milne 1995). High Energy Spectroscopic System (H. E.S.S.) observations of N132D classify this radio-loud SNR as one of the strongest emitters of γ rays in the LMC (H.E.S. S. Collaboration et al. 2015; Ackermann et al. 2016). It has been estimated that N132D has converted up to 17% of its explosion energy into accelerating cosmic rays (H.E.S.S. Collaboration et al. 2015). N132D is also the brightest SNR among all the known SNRs in the 1–100 GeV band (Acero et al. 2016). There is evidence for active star formation in the vicinity of N132D, as observed in the Hα images from the Magellanic Cloud Emission-Line Survey (MCELS; Smith & MCELS Team 1999; Smith et al. 2004), but no young stellar objects (YSOs) have been detected in the molecular cloud interacting with the SNR (Desai et al. 2010; see also, Danziger & Dennefeld 1976).

Chandra X-ray Observatory (Chandra) observations (Borkowski et al. 2007) reveal a well-structured rim running along the southern part of the remnant (see Figure 1). This well-defined rim is associated with dense molecular clouds in this direction (Banas et al. 1997; Sano et al. 2015) and is also present in the infrared (IR) observations of dust continuum emission in N132D taken by Spitzer (Williams et al. 2006). Using IR data from Spitzer and Herschel Space Observatory (Lakićević et al. 2015), it has been proposed that the X-ray-emitting hot plasma has destroyed almost half of the dust grains in the remnant (Tappe et al. 2006, 2012; Seok et al. 2013; Dopita et al. 2018; Zhu et al. 2019). The X-ray emission also shows a bright arc-shaped structure close to the outermost shell in the south and southeast that may be attributed to the reverse shock encountering the ejecta or face-on filaments produced by the forward shock interacting with density enhancements in the surrounding medium. Toward the north, there are filament-like structures protruding outward that are relatively faint in X-rays as compared to the rest of the remnant.

---

[5] The quoted X-ray luminosity is uncorrected for LMC absorption.
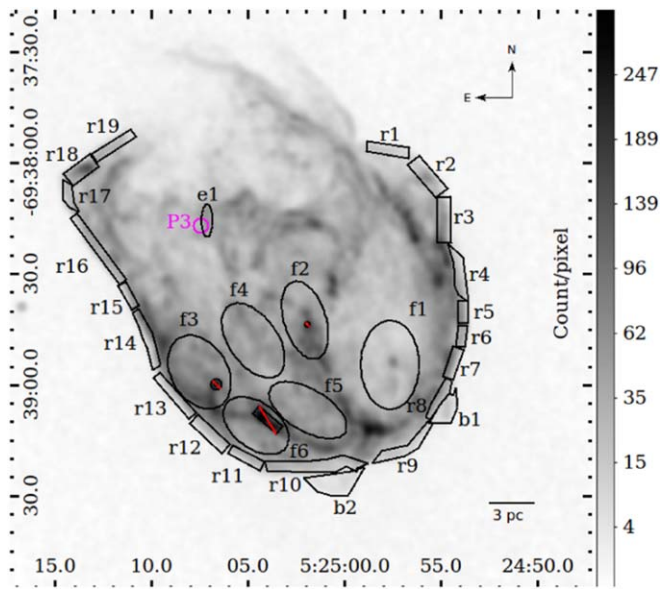
Figure 1. Chandra ACIS-S image of counts per pixel in N132D in the 0.35–7.0 keV band with x and y axes showing the R.A. and decl., respectively. One pixel is $0''5$, where $1'' = 0.24$ pc. The gray scale has been inverted so that a darker shade corresponds to higher counts. All regions studied in this work are indicated by black polygons with labels: r1–r19 are the rim regions and b1–b2 are the two likely protrusions beyond the blast wave. In the interior, we study regions e1 (which has enriched abundances of O, Ne, Mg, Si, and Fe) and f1–f6 (where weak Fe K emission is detected). Black areas with a red strikethrough line within regions f2, f3, and f6 are the bright patches affected by pileup that are excluded from the spectroscopic analysis. P3 is an O-rich region found in optical studies of N132D by Morse et al. (1996, 1995) and Blair et al. (2000).

Given that these structures are at the edge of the H I cloud (Kim et al. 2003) that encompasses the remnant (Maggi et al. 2016, see their Figure 12), they may have resulted from strong shocks breaking out of the cavity into the ambient ISM.

Although N132D is the brightest SNR in the LMC in X-ray, a full spectral analysis of the archival Chandra data (Borkowski et al. 2007) has not yet been performed. In this work, we carry out a spatially resolved analysis of the well-defined rim and of several interesting regions in the interior of the remnant that collectively cover about one-third of the remnant in projection. We assume the distance to N132D to be 50 kpc in all calculations hereafter (Clementini et al. 2003; Pietrzyński et al. 2013, 2019). At this distance, $1'' = 0.24$ pc. We describe the data reduction and processing in Section 2 and source and background models used for spectral analysis of all regions in Section 3. Section 4 gives the resulting fits. We discuss the results in Section 5 and summarize our analysis in Section 6.

2. X-Ray Data and Reduction

We use X-ray observations of SNR N132D obtained with the S3 chip in Chandra's Advanced Charged Couple Device (CCD) Imaging Spectrometer (ACIS-S) detector array (Bautz et al. 1998). N132D was observed for 89 ks by Chandra (Borkowski et al. 2007) in three ACIS-S observations in the Very Faint mode (see Table 1). These X-ray observations showed the parsec-scale substructure in the previously known roughly elliptical shape ($\sim$14.8 $\times$ 10.9 pc) in exquisite detail. We find no flaring in the data after examining the light curves of the observations. However, the X-ray data suffer from pileup

Table 1
Chandra ACIS-S Observation Log of SNR N132D

ObsID	Observation Date	Exposure (ks)	R.A.	Decl.	Roll
05532	2006 Jan 09	44.59	$81°2595$	$-69°6437$	$330°2$
07259	2006 Jan 10	24.85	$81°2595$	$-69°6437$	$330°2$
07266	2006 Jan 15	19.90	$81°2595$	$-69°6437$	$330°2$

in certain regions (Ballet 1999; Davis 2001). We show a map of the pileup in the remnant in Appendix A. For certain bright areas in the regions in the interior where pileup is greater than 10%, we exclude them from the fit. We utilize the X-ray analysis package Chandra Interactive Analysis of Observations (CIAO version 4.9, Fruscione et al. 2006) and the Chandra Calibration Database (CALDB, version 4.7.3, Graessle et al. 2007). We use Xspec version 12.9.1 k (Arnaud 1996) to perform X-ray spectroscopy in various regions in the remnant. The line emission data is taken from AtomDB version 3.0.7 (Foster et al. 2013), whereas the nonequilibrium ionization (NEI) models come from NEI version 3.0.4. We use the cosmic abundance set by Wilms et al. (2000) as the baseline abundance level for all of our analysis.

3. Spectral Analysis

We first analyze the well-defined rim of SNR N132D to get a picture of emission from the forward shock. We number the rim regions r1–r19 in the clockwise direction, as we show in Figure 1. We also identify and analyze two "blobs" (labeled b1 and b2) that are likely protruding ahead of the forward shock. We then search the entire remnant for regions that show possibly enhanced abundances of one or more elements, through visual inspections of narrowband images centered on line features of O, Ne, Mg, Si, S, and Fe (see Appendix A), as well as hardness ratio images in the soft (0.3–0.9 keV), medium (0.9–2 keV), and hard (2–7 keV) bands. We select interior regions e1, f1, f2, f3, f4, f5, and f6 for further study (see Sections 3.2.2 and 3.2.3 for additional details). We note that regions f2, f3, and f6 contain bright areas in projection that are significantly affected by pileup, as shown in Figure A1. We exclude such areas when performing X-ray spectroscopy on these regions. Table 2 lists the classification of each region together with the location of its center and area. The following subsections describe the background and source models we use to fit the background and source spectra, respectively.

3.1. Background Model

The background region we select is a $1'62$ square located at R.A. = 05:24:36.963, decl. = −69:37:05.68 at a distance of $2'74$ from the remnant. We do not subtract the background spectrum from each source spectrum; rather, we model it separately because of the low number of counts at energies >2.5 keV. With low counts, the subtraction of Poisson distributions results in a distribution that is non-Poissonian and far from Gaussian; in addition, the number of counts after subtraction can be negative (see, for example, van Dyk et al. 2001; Garofali et al. 2017).

We differentiate the background model into sky (imaged through the X-ray optics) and detector (not imaged through the optics) components. For the detector background model, we analyze the so-called "stowed" background data in the Very

Table 2
Classification of All Regions Shown in Figure 1

Region	Location	R.A.	Decl.	Area (pc²)
r1	Rim	5:24:57.753	−69:37:56.60	1.93
r2	Rim	5:24:55.700	−69:38:03.86	2.84
r3	Rim	5:24:54.851	−69:38:15.55	2.51
r4	Rim	5:24:54.186	−69:38:30.42	2.99
r5	Rim	5:24:53.824	−69:38:40.57	0.96
r6	Rim	5:24:53.929	−69:38:46.91	0.82
r7	Rim	5:24:54.364	−69:38:54.15	1.49
r8	Rim	5:24:55.145	−69:39:04.67	1.81
r9	Rim	5:24:56.799	−69:39:16.15	6.37
r10	Rim	5:25:01.193	−69:39:21.65	6.29
r11	Rim	5:25:05.082	−69:39:19.87	1.48
r12	Rim	5:25:06.968	−69:39:13.36	2.22
r13	Rim	5:25:08.805	−69:39:03.01	2.10
r14	Rim	5:25:10.241	−69:38:47.50	2.73
r15	Rim	5:25:11.173	−69:38:36.08	1.01
r16	Rim	5:25:12.741	−69:38:23.41	2.75
r17	Rim	5:25:14.211	−69:38:09.52	1.29
r18	Rim	5:25:13.631	−69:38:02.10	2.17
r19	Rim	5:25:11.931	−69:37:55.47	1.91
b1	Blob	5:24:54.730	−69:39:05.84	4.05
b2	Blob	5:25:00.428	−69:39:26.84	6.36
e1	Interior	5:25:07.105	−69:38:15.80	1.21
f1	Interior	5:24:58.031	−69:38:42.24	17.51
f2	Interior	5:25:03.585	−69:38:44.65	11.20
f3	Interior	5:25:07.744	−69:38:56.73	14.49
f4	Interior	5:25:04.716	−69:38:48.14	13.74
f5	Interior	5:25:01.888	−69:39:06.96	12.23
f6	Interior	5:25:04.575	−69:39:11.08	10.16

Note. The R.A. and decl. coordinates mark the centers of each region. All of the rim regions have at least 3500 X-ray photon counts within 0.3–7.0 keV.

Faint mode to construct a spectral model for the S3 CCD, similar to the approach used for the ACIS-I CCDs by Bartalucci et al. (2014). We download the background data set acis7D2005-09-01bgstow_ctiN0002.fits from the CALDB. We then run `acis_process_events` to populate the `TDETX` and `TDETY` columns. After copying over the status column from acis7D2005-09-01bgstow_ctiN0002.fits to the processed file (since `acis_process_events` zeroed the status column), we apply the CIAO tool `reproject_events` using ObsID 05332 as the match file to project the background events onto the sky. We extract the detector background from the same region as used for the sky background (see below) and generate a weighted `RMF` using a `WMAP` in `TDET` coordinates. The detector background model consists of a broken power law (`bkn2pow`) to represent most of the spectrum from 0.3 to 11.0 keV, with a broad Gaussian to account for the high-energy ACIS-S3 background continuum. We include Gaussian lines for the instrumental fluorescence lines (Al Kα, Si Kα, Au M complex, Ni Kα, and Au Lβ). We initially adopt the line energies from Bearden (1967), subsequently thawing the line energy for Si Kα, the Au M complex, Ni Kα, and the Au Lβ complex. We also thaw the line width for Au M and Au Lβ complexes. Once a good fit is found, we freeze all of the parameters and thaw a multiplicative `const` parameter (initially frozen at 1.0) that provides an overall normalization scaling.

The sky model consists of an absorption (`tbabs`) plus two thermal plasma `apec` (∼0.2 keV and ∼0.8 keV) components and a power law. The 0.19 keV `apec` model primarily represents emission from the local hot bubble (LHB), and the 0.77 keV model represents other Galactic and LMC emission along the line of sight and the Galactic Halo (Snowden et al. 1998, 2008). There may be emission from the LHB that contributes to the emission we model with the 0.77 keV plasma model, and there may be emission from the Halo that contributes to the emission we model with the 0.19 keV plasma model (Snowden et al. 1997; Kuntz & Snowden 2001; McCammon et al. 2002; Kavanagh et al. 2020). This is not an issue for us as we require an empirical model for the background. We use the `powerlaw` component with a fixed slope of 1.46 (Chen et al. 1997; Snowden et al. 2004; Kuntz & Snowden 2010) to model the cosmic X-ray background from unresolved point sources including active galactic nuclei (AGNs). We fit the sky model using the absorbed thermal models and power law, together with the detector background model (described above). In the fitting, we allow the detector background `const` parameter to vary, but otherwise, we fix the shape of the detector background; the fit is performed over 0.30–11.0 keV. Once a good fit is obtained, we freeze the sky model parameters and allow a multiplicative `const` factor (initially frozen at 1.0) to vary.

When fitting a source spectrum, we freeze the parameters that affect the detector and sky background model shapes while allowing the overall normalizations to vary through multiplicative constants for the detector and sky backgrounds (see, for example, Maggi et al. 2016; Garofali et al. 2017). Table 3 presents the background model and Figure 2 shows the background fit. As we show in Sections 4.1 and 4.2.1, the background is significantly lower than the source spectra in the interior as well as on the rim, respectively, for most of the bandpass except at the highest energies ($E > 5.5$ keV).

3.2. Source Models

For all of the (source) regions we analyze in this work, we take a two-component absorption model to account for Galactic (`tbabs`) and LMC (`tbvarabs`) absorption by gas, molecules, and grains along the line of sight. Following Dickey & Lockman (1990), we fix the Galactic hydrogen column density $N_{\rm H,Gal}$ to 5.5×10^{20} cm^{-2} with solar abundances (Wilms et al. 2000), whereas we allow the LMC hydrogen column density to vary. For all spectral fits, we set the initial guess for LMC elemental abundances to be $0.4\times$ solar on the Wilms et al. (2000) scale, in line with the estimated metallicity of the LMC (Dufour et al. 1982; Russell & Dopita 1992; Westerlund 1997). Due to the limited number of counts in the energy range 0.3–0.5 keV in our spectra, where emission from C and N is prominent, we tie the C and N abundances to O in the source models. Similarly, due to poor constraints on the abundances of S, Ar, and Ca and the possibility of the L-shell emission of these elements affecting fits at lower energies, we tie them together. We cannot constrain the abundance of Ni with the current data because of the low number statistics, and we tie it to that of Fe. For all fits, we utilize the energy range between 0.3 and 7.0 keV, except for the regions where we study Fe K emission and extend the fit to 7.5 keV (see Section 3.2.3 for details).

With the angular resolution of Chandra, we can separate the forward shock from the rest of the remnant along the rim. We fit the rim regions with a plane-parallel shock model (`vpshock`; see Borkowski et al. 2001) because we expect to find a shock running into relatively cold and mostly neutral

Table 3
Best-fit Parameters of the Background Model Consisting of the Detector and Sky Components

Component	Parameter	Units	Value
Detector	bkn2powPhoIndex1	...	$1.60^{+1.17}_{-0.58}$
	bkn2powBreakE1	keV	$0.50^{+0.03}_{-0.03}$
	bkn2powPhoIndex2	...	$0.46^{+0.03}_{-0.03}$
	bkn2powBreakE2	keV	$4.58^{+0.70}_{-0.49}$
	bkn2powPhoIndex3	...	$1.51^{+0.70}_{-0.54}$
	bkn2powNorm	photons keV^{-1} cm^{-2} s^{-1}	$1.433^{+0.001}_{-0.001} \times 10^{-3}$
	Gaussian1 LineE	keV	$11.314^{+0.226}_{-0.188}$
	Gaussian1 Sigma	keV	$1.954^{+0.145}_{-1.23}$
	Gaussian1 Norm	photons cm^{-2} s^{-1}	$6.893^{+0.008}_{-0.007} \times 10^{-2}$
	Gaussian2 LineE	keV	1.487
	Gaussian2 Sigma	keV	0.0
	Gaussian2 Norm	photons cm^{-2} s^{-1}	$3.868^{+3.680}_{-3.476} \times 10^{-5}$
	Gaussian3 LineE	keV	$1.860^{+0.007}_{-0.012}$
	Gaussian3 Sigma	keV	0.0
	Gaussian3 Norm	photons cm^{-2} s^{-1}	$4.650^{+0.573}_{0.055} \times 10^{-4}$
	Gaussian4 LineE	keV	$2.212^{+0.012}_{-0.123}$
	Gaussian4 Sigma	keV	$0.060^{+0.028}_{-0.019}$
	Gaussian4 Norm	photons cm^{-2} s^{-1}	$5.070^{+0.808}_{-0.698} \times 10^{-4}$
	Gaussian5 LineE	keV	$7.555^{+0.019}_{-0.008}$
	Gaussian5 Sigma	keV	0.0
	Gaussian5 Norm	photons cm^{-2} s^{-1}	$3.648^{+0.580}_{-0.555} \times 10^{-4}$
	Gaussian6 LineE	keV	$9.853^{+0.030}_{-0.017}$
	Gaussian6 Sigma	keV	$0.050^{+0.030}_{-0.050}$
	Gaussian6 Norm	photons cm^{-2} s^{-1}	$8.780^{+1.649}_{-1.552} \times 10^{-4}$
Sky	TBabsN_{H}	cm^{-2}	$0.186^{+0.132}_{-0.052} \times 10^{21}$
	apec1 kT_{e}	keV	$0.175^{+0.009}_{-0.023}$
	apec1 Norm	cm^{-5}	$1.578^{+3.001}_{-0.427} \times 10^{-4}$
	apec2 kT_{e}	keV	$0.768^{+0.040}_{-0.051}$
	apec2 Norm	cm^{-5}	$3.097^{+1.002}_{-0.431} \times 10-5$
	powerlawPhoIndex	...	1.46
	powerlawNorm	photons keV^{-1} cm^{-2} s^{-1}	$3.404^{+1.049}_{-1.346} \times 10^{-6}$

Note. Errors represent the 68% confidence intervals, which correspond to 1σ in the Gaussian case. Parameters without errors were frozen in the fit.
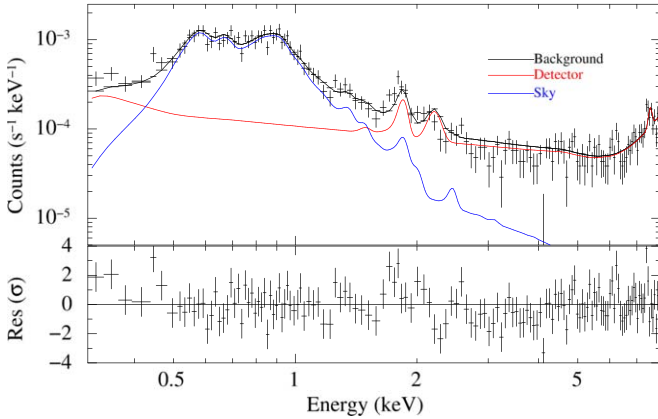
Figure 2. Background spectrum and model between 0.3 and 8.0 keV. The background model (black) is a mixture of detector (red) and sky (blue) components. The detector component consists of a broken power law (bkn2pow) and multiple Gaussians, whereas the sky component consists of two thermal (apec) models and a powerlaw model. The thermal models dominate from 0.5 to 1.0 keV, and the detector background dominates above 2.0 keV. The background becomes significant above 5.5 keV.

material. This model loses its accuracy when the conditions in the emitting region depart significantly from its assumptions, for example, when the temperature or density varies across the region, or the material is already heated by previous shocks or thermal conduction (Hamilton et al. 1983; Jones & Ellison 1991). Consequently, we add an NEI component (vnei) to the model to explain emission from plasma heated to some temperature and evolved for a particular time (τ), while not including emission from earlier times (see, for example, Masai 1994; Borkowski et al. 2001; Ellison et al. 2007). It also allows for the possibility of the detection of ejecta fragments if we allow the abundances of the vnei component to vary. In cases where the source model consists of more than one component, we start the fit by fixing the abundances of one or more vnei components to be the same as that of the vpshock component.

Apart from the vpshock and vnei models, we also investigate the case of a recombining plasma that may be responsible for emission in the Fe K complex. In the case of a recombining plasma, the ionization temperature of ions exceeds the electron temperature (McKee 1974; Itoh 1977). We use the nonequilibrium plasma model vrnei, which is a modified version of vnei in which the initial temperature (kT_init) can be specified; the model starts in collisional ionization equilibrium at kT_init, the temperature is changed to kT, and the ionization state evolves at constant kT and density. A vrnei with kT_init set to 0.0808 keV is equivalent to

vnei. If `kT_init` exceeds `kT`, the model evolves by recombining. As with `vnei`, the emission is calculated at a specific value of τ. We describe this further in Section 3.2.3. In the following subsections, we lay out the fitting algorithms for the different regions we analyze.

3.2.1. Rim Regions

We define rectangular regions on the rim wherever possible; some regions are distorted in shape to account for the locally nonuniform curvature of the remnant. All of the regions around the rim (r1–r19, b1–b2) have nearly the same width (0.6–0.7 pc) and have at least 3500 counts in the 0.3–7.0 keV bandpass. We use the following procedure to fit the rim regions and the blobs:

1. Fit the spectrum of a region on the rim with a source model (`tbabs × tbvarabs × vpshock`), with abundances fixed at 0.4× solar (Borkowski et al. 2007).
2. If the fit is acceptable in step 1 (following the criteria we describe in Section 3.3), note the abundances.
3. If the fit is not acceptable, allow the abundances of O, Ne, Mg, Si, S, and Fe to vary one by one. If it is acceptable after the abundances have been allowed to vary, note the best-fit abundances and error bars.
4. Fit all of the regions on the rim in the same manner. After this step, all regions would have been fitted once with `vpshock`.
5. Find an average abundance for each element from regions where the fit in steps 1 or 3 was acceptable.
6. Refit the regions where the fit was not acceptable in steps 1 or 3 with the mean abundances calculated in step 5.
7. If the fit is still not acceptable in step 6, add an NEI component (`vnei`) to the source model and refit.

As we show in Section 4.1, for the two regions on the rim where a single `vpshock` did not generate an acceptable fit, the two-component model satisfactorily fits the spectra. Thus, we do not go beyond step 7 to fit any region on the rim. Finally, to calculate the mean local LMC abundances for all elements, we add an additional step in the algorithm in which we fit all of the rim spectra with the abundances of O, Ne, Mg, Si, S, and Fe free. This is necessary to get meaningful uncertainties on the average abundances that would otherwise be underestimated if some elemental abundances were held fixed in some regions (Maggi et al. 2019).

3.2.2. Region e1

We examine the O-rich ring seen in the optical in N132D (Morse et al. 1995; Blair et al. 2000), also called Lasker's Bowl, as an interior region that might exhibit enriched abundances in the X-ray spectral data. The presence of ejecta-rich knots in X-rays in this ring was previously reported by Borkowski et al. (2007, see their Figure 2). We select region e1 on this ring, which overlaps with both the ejecta-rich knots marked in the X-ray data and the O-rich ejecta seen in the optical. The spatial coincidence of optical O-rich ejecta and X-ray enhancements in O, Ne, Mg, Si, and Fe emission points to e1 being a complex region in which multiple components with different plasma conditions are contributing. Moreover, its location also overlaps with a region that shows O- and Ne-rich ejecta in the 14–36 μm infrared map of N132D (Tappe et al. 2012, see their region I in Figure 1). To fit this region, we use

an NEI component (`vnei`) and add a `vpshock` component to account for the shell emission.

3.2.3. Regions with Fe K Emission

N132D is one of the few extragalactic SNRs for which direct measurements of the spatial distribution of Fe-rich ejecta can be made. The Fe Kα complex ranges from 6.4 keV for neutral Fe to 7.0 keV for Fe XXVI. The spectrum of the entire remnant indicates a peak in emission at ~6.7 keV (presumably Fe XXV emission). A center-filled excess of Fe K emission was detected in the observations of N132D taken by XMM-Newton (Behar et al. 2001), but Chandra data reveal that the extent of this emission is spread largely across the southern part of the remnant. As we show in Figure 3, we create three 0.4 keV wide passbands to sample this Fe K emission and the surrounding continuum: 6.1–6.5, 6.5–6.9, and 6.9–7.3 keV (see also Figure A2). We then select six large regions (f1–f6) to study the Fe K emission feature in this remnant. We select enough regions such that they collectively sample the majority of the Fe K counts observed in the spectrum, and we exclude areas where the pileup fraction is high, as shown in Figure A1. The analysis of a single spectrum from the entire southern half of the remnant combines data from regions with different plasma conditions such that a complex, multicomponent model is necessary to represent the data. Thus, it is more meaningful to analyze the spectra on smaller spatial scales in which the inherent variations in the plasma conditions are smaller.

For regions where we study emission from Fe K lines, we fit the spectra in the energy range 0.3–7.5 keV to sufficiently sample the continuum on either side of the feature at 6.7 keV. We present analyses based on both ionizing and recombining plasma models for regions f1–f6. SNRs interacting with molecular clouds are frequently associated with recombining plasma, although the mechanism that produces the recombining plasma is not clear. One possibility is thermal conduction between the remnant shell and the cloud as suggested by Rho & Petre (1998). Commonly quoted evidence for this scenario is the anticorrelation between electron temperature and recombining timescale (e.g., Katsuragawa et al. 2018; Okon et al. 2018, 2020). On the other hand, an overionization of the plasma is possible if the shock evaporates the cloud (White & Long 1991). Itoh & Masai (1989) and Yamaguchi et al. (2009) suggest that an overionized plasma may be produced by rapid adiabatic expansion if the shock propagates from a region of high density to a region of low density (Shimizu et al. 2012). In this scenario, a positive correlation is observed between the electron temperature and the recombining timescale (e.g., Yamaguchi et al. 2018). Detailed simulations of the X-ray emission from an SNR shock interacting with a distribution of clouds in the ISM conducted by Zhang et al. (2019) show that both thermal conduction and adiabatic expansion are likely to produce radiative recombination emission at different locations in the remnant (see also Zhou et al. 2011).

Nonequilibrium ionization in SNRs typically manifests itself as (1) an ionizing plasma or (2) a recombining plasma. In the first case, the plasma is underionized; the ionization stages and line ratios reflect an ionization temperature $kT_z < kT_e$. The plasma evolves via ionization, and the radiative recombination continuum (RRC) features are weak. In the second case, the plasma is overionized, and the ionization stages and line ratios reflect $kT_z > kT_e$. The plasma evolves via recombination and has strong RRC features, with the continuum featuring
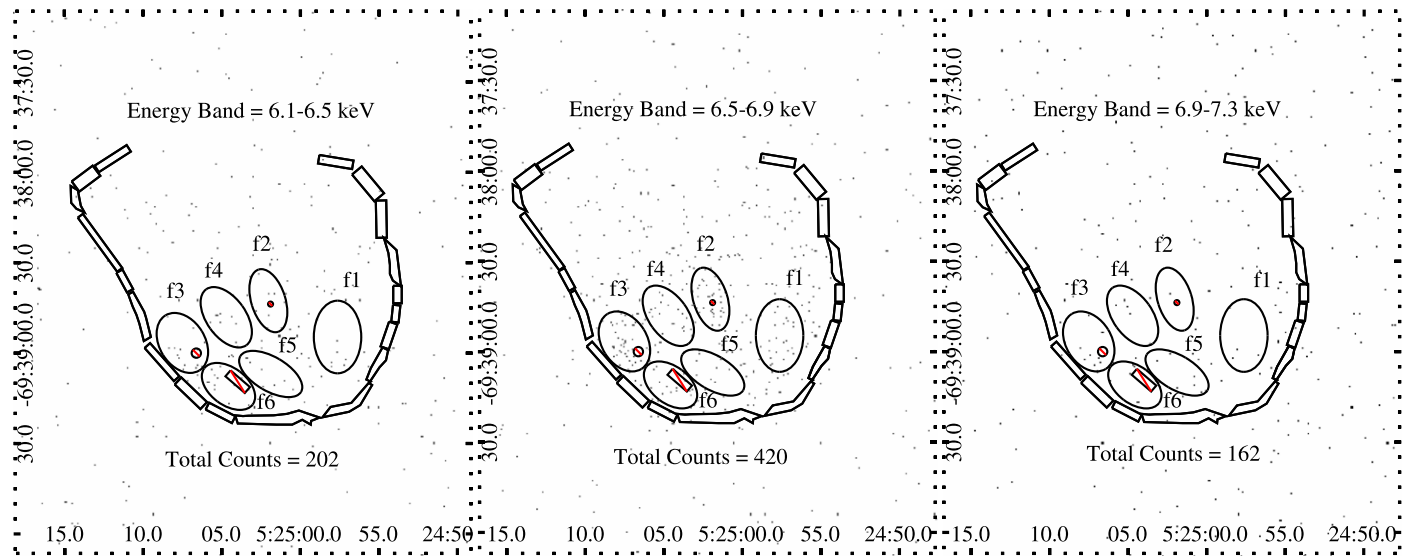
Figure 3. Spatial distribution of counts in the energy range 6.1–7.3 keV in N132D. From left to right, images are shown for energy ranges 6.1–6.5, 6.5–6.9, and 6.9–7.3 keV, respectively. Rim regions mark the extent of the remnant. The middle panel shows emission from He-like Fe Kα (∼6.7 keV), while the adjacent lower and higher energy bands indicate the continuum levels. The middle energy band shows a significant excess compared to the continuum.

sawtooth-like excesses extending upward in energy from the ionization potential, and line ratios exceeding the expectations for collisional ionization equilibrium due to a radiative cascade populating higher levels.

The basic ionizing plasma versus recombining plasma features for SNR spectra have been long understood (Itoh 1977; Mewe & Gronenschild 1981; Gaetz 1990; Masai 1994). The shocking of low-temperature material results in ionization to more excited states. Eventually adiabatic cooling dominates as the remnant expands. Ultimately the plasma becomes over-ionized, with a recombining plasma. The surprising aspect of recent discoveries of recombining plasmas was that the plasmas are strongly recombining, with kT_z greatly exceeding kT_e with significant radiative RRCs and significant line ratio and ionization state anomalies. Kawasaki et al. (2002) proposed an overionized plasma based on anomalous line ratios in Advanced Satellite for Cosmology and Astrophysics (ASCA) observations of SNR IC 443. The existence of strongly recombining plasmas in SNRs was established by Yamaguchi et al. (2009) with the discovery of radiative recombination continua (RRCs) of H-like Si and S in Suzaku observations of SNR IC 443 and of H-like Fe in Suzaku observations of SNR N49B by Ozawa et al. (2009).

The strength of the RRC emission depends on the electron temperature, the ion temperature, and the ionization timescale (see Yamaguchi et al. 2009 for a discussion). The presence of hot, He-like Fe plasmas in N132D is suggestive of recombining plasma. The Fe K RRC feature in the Chandra spectra is difficult to disentangle from systematic instrument character-istics like decreasing effective area and increasing detector background at $\gtrsim 7$ keV, and the ability to detect excess Kβ over Kα is also limited by the CCD spectral resolution and the low sensitivity achieved in the ∼90 ks of available data. In principle, Hitomi Collaboration et al. (2018) observations of N132D with low background could potentially be used to constrain the H-like Kα to He-like Kα ratio, which can provide evidence for a recombining plasma (Kawasaki et al. 2002; Porquet et al. 2010; Lopez et al. 2013). However, the low

number of counts in the Hitomi spectrum makes such an analysis challenging and beyond the scope of this paper. As we show in Section 4.2.2, it is thus not possible to provide a definitive case for the existence of a hot Fe K emitting recombining plasma in the remnant. Nevertheless, we examine this case as a possible alternative to the ionizing case.

For the case of an ionizing plasma, we introduce a two-component `vnei`, where the cooler component explains the soft X-ray spectrum and Fe L emission, and the hotter component explains the hard X-ray spectrum and Fe K emission. For the case of a recombining plasma, we use the recombining collisional plasma model `vrnei`, together with a `vnei` that can account for the low-temperature plasma. Both models also contain a `vpshock` component to represent the shell emission along the line of sight. As we show in Section 4.2.2, such three-component models (`vnei/vrnei` + `vnei` + `vpshock`) are necessary to account for the Fe K emission in these regions.

3.3. Fit Evaluation

We use the C-statistic (which approximates the Poisson log-likelihood) to evaluate the spectral fits because it does not introduce a bias in the case of a low (or null) number of counts per spectral bin (Cash 1979; Nousek & Shue 1989; Leccardi & Molendi 2007). We further use the goodness-of-fit criterion developed for the C-statistic by Kaastra (2017), by comparing the observed value of the C-statistic (`cstat(O)`) with the expected value (`cstat(E)`) and expected variance deter-mined from the predicted model counts in each bin, using the numerical estimates derived by Kaastra (2017). We show both the expected value and the width of the distributions that would result when the fit is good. We adopt the following criterion to determine if a fit is acceptable if `cstat(E)` $-2.6\sigma_E <$ `cstat(O)` $<$ `cstat(E)` $+ 2.6\sigma_E$, where σ_E^2 is the expected var-iance of `cstat(E)`, and we choose the bounds such that the probability that `cstat(O)` falls outside the range is 1%.

4. Results

4.1. Rim Regions and Blobs

Using the fit evaluation criteria we outline in Section 3.3, we find that spectral analyses of 17 out of the 19 rim regions produce an acceptable fit with the single-component vpshock model, which we summarize in Table 4. For the two regions where the single-model fit fails, we redo the fitting while adding a vnei component. We present the results for the two-component model in Table 5.

Table 6 shows the mean abundance values (μ, with $1\sigma_\mu$ errors) we calculate for the rim and the scatter in each parameter. We emphasize that the mean values we calculate are from fitting the abundances of O, Ne, Mg, Si, S, and Fe in all of the rim regions; this prevents a bias in the estimate of the mean that can arise due to some fits having some parameters frozen. We follow the method of Multiple Imputations (Lee et al. 2011) to find the error on the mean (σ_μ) and the scatter, which takes into account the statistical as well as systematic uncertainties (in other words, within and between variance). We present the details of this method in Appendix B. If the scatter in an elemental abundance along the rim is <1 (implying that there is more systematic than statistical error), we consider its variation to be insignificant. If the best-fit abundance and associated 1σ error in any region on the rim is more than $\mu + \sigma_\mu$ or less than $\mu - \sigma_\mu$, we classify it as being enhanced or reduced, respectively.

A single-component vpshock model provides an adequate fit (evaluated using the criteria described in Section 3.3) for regions r1, r2, r4–r9, r11–r19, b1, and b2. Figure 4 shows the spectral fit with this model for region r1, along with the background to emphasize that the background counts are significantly less than the source counts (see Figures C1–C10 in Appendix C for all other spectral fits of the rim regions and the blobs). However, some peculiarities are noticeable in the fits: regions r1 and r2 show systematic residual deviations around 1.5–2 keV and 0.5–0.6 keV, respectively; r6 and r7 show excess Fe; r11 underpredicts the flux near 1.2 keV; r13–r15 require a lower abundance of Mg; r14 is also under-abundant in O, Ne, and Si; r16 shows higher than mean levels of S, and r17 shows enhanced S; b1 is consistent with excess Fe; and b2 appears to contain ambient ISM material. Regions r3 and r10 are poorly fit with this model, and we refit them with the more complex vpshock+vnei model. We find that these regions show an additional plasma component with a higher temperature than the shell emission, which has been recently excited given their low ionization timescales. Unlike the single-component fits, the difference between cstat(O) and cstat(E) is well within the $2.6\sigma_E$ limit.

Figure 5 depicts the trends seen along the rim in the parameters of interest for the single vpshock model. We see the column density along the line of sight (N_H) is higher in the southern part of the remnant than in the western and eastern parts, which corresponds to presumably denser material (molecular clouds) being present in that direction, as has been observed in the NANTEN CO survey (Fukui et al. 2008), the Magellanic Mopra Assessment (MAGMA) survey of CO in the LMC with the Mopra telescope (Wong et al. 2011), and high-resolution ALMA observations of N132D (Sano 2019). In fact, many southern rim regions spatially coincide with the locations of shocked ISM clouds found by Dopita et al. (2018, see their Figure 2) in the optical. The ionization timescale (τ) is roughly

uniform over the shell, and its values are indicative of a nonequilibrium plasma.

Figure 6 shows the abundance pattern across the rim for O, Ne, Mg, Si, S, and Fe. Note that the fit results plotted in Figure 6 are not the same as in Table 4, as we explain above. The shaded areas correspond to $1\sigma_\mu$ deviations from the mean abundance value, where σ_μ accounts for the statistical and systematic uncertainty around the mean. The thick dashed lines mark the mean value. We can summarize the results as follows:

1. O: The abundance of O is uniform along the rim, except in region r2, where it is enhanced.
2. Ne: The abundance of Ne is within σ_μ of the mean throughout the rim.
3. Mg: The scatter in the abundance of Mg is <1, implying that the variance between the different measurements is less than that within the measurements.
4. Si: The abundance of Si is also uniform across the rim, but the scatter is more than one, implying the presence of localized variations. Further, region r8 is marginally consistent with the average.
5. S: We are cautious while thawing the abundance of S in the fits, because of the caveats listed in Section 3. Although it is poorly constrained on the rim regions, due to low counts, region r17 shows a significant enhancement. The scatter in S is greater than 1, again implying the presence of localized variations.
6. Fe: The abundance of Fe is uniform over the rim. Like Mg, the scatter in the abundance of Fe is less than 1.

Based on our spectral analysis and the evaluation criteria for enhanced/reduced abundance measurements, we find that the abundances are largely uniform around the rim. The two exceptions to this are the enhanced O on the northwestern rim (region r2) and S on the northeastern rim (region r17).

4.2. Interior Regions

In this section, we describe results from the spectral analysis of the interior regions e1 and f1–f6, which were selected from narrowband (see Figure A2) and hardness ratio images as having enhanced abundances and signatures of Fe K emission, respectively.

4.2.1. Region with Enriched Abundances

Table 5 shows the fit results for region e1, and Figure 7 shows the source spectra with the best-fit model. The results reveal enriched abundances ($\gtrsim 2.5\times$ mean) of all elements (except S) in this region, consistent with the excess flux at different line energies we observe in the narrowband images. Adding a single NEI component to the model fits the observed spectrum well with an electron temperature of ~2.0 keV. The higher temperature of the vnei as compared to the shell emission from the rim implies the presence of one or multiple shock-heated ejecta clumps in this region. The shorter ionization timescale indicates that the ejecta-rich clump(s) present in this region have been recently heated by the shock. The best-fit abundances have large uncertainties because of the low number of counts. Nevertheless, they are significantly higher than the LMC abundances. We use the best-fitting parameters from the fit for this region to deduce the mass of the progenitor in Section 5.3. The coeval presence of optical and X-ray-emitting ejecta in a region has also been observed in

Table 4
Fit Results of Plane-parallel Shock Model (vpshock) on Rim Regions and Blobs

| Region ID (1)	N_H (2)	kT_e (3)	τ (4)	norm (5)	O (6)	Ne (7)	Mg (8)	Si (9)	S (10)	Fe (11)	cstat(O)/dof (12)	cstat(E) $\pm \sigma_E$ (13)
...	10^{22} cm^{-2}	keV	10^{11} cm^{-3} s	10^{-4} cm^{-5}	...	...	...	...	...	...	...	...
r1	$0.05^{+0.02}_{-0.02}$	$1.22^{+0.11}_{-0.08}$	$0.60^{+0.10}_{-0.09}$	$0.66^{+0.03}_{-0.04}$	0.46	0.59	0.44	$0.84^{+0.17}_{-0.15}$	0.40	0.29	816/911	778 ± 41
r2	$0.06^{+0.01}_{-0.01}$	$0.92^{+0.07}_{-0.04}$	$1.78^{+0.45}_{-0.38}$	$2.17^{+0.19}_{-0.29}$	$0.78^{+0.18}_{-0.13}$	0.59	$0.64^{+0.11}_{-0.09}$	$0.70^{+0.10}_{-0.11}$	0.40	$0.45^{+0.10}_{-0.08}$	869/908	802 ± 42
r3*	$0.08^{+0.01}_{-0.01}$	$0.75^{+0.03}_{-0.03}$	$2.12^{+0.25}_{-0.23}$	$6.03^{+0.39}_{-0.38}$	0.46	$0.46^{+0.03}_{-0.04}$	0.44	0.52	$0.81^{+0.20}_{-0.09}$	$0.32^{+0.03}_{-0.02}$	939/909	803 ± 42
r4	$0.09^{+0.02}_{-0.02}$	$0.82^{+0.03}_{-0.03}$	$1.79^{+0.21}_{-0.20}$	$2.57^{+0.13}_{-0.11}$	0.46	$0.54^{+0.05}_{-0.05}$	$0.49^{+0.06}_{-0.06}$	0.52	$0.82^{+0.28}_{-0.24}$	0.29	826/909	782 ± 42
r5	$0.09^{+0.02}_{-0.02}$	$0.71^{+0.02}_{-0.02}$	$3.29^{+0.38}_{-0.33}$	$2.35^{+0.08}_{-0.10}$	0.46	0.59	0.44	0.52	$0.75^{+0.30}_{-0.25}$	0.29	823/911	750 ± 41
r6	$0.15^{+0.03}_{-0.02}$	$0.82^{+0.11}_{-0.05}$	$1.82^{+0.48}_{-0.64}$	$1.45^{+0.19}_{-0.29}$	0.46	0.59	$0.59^{+0.12}_{-0.08}$	0.52	0.40	$0.37^{+0.10}_{-0.05}$	744/910	747 ± 40
r7	$0.06^{+0.01}_{-0.01}$	$0.80^{+0.04}_{-0.04}$	$2.70^{+0.42}_{-0.40}$	$3.16^{+0.22}_{-0.26}$	0.46	$0.48^{+0.19}_{-0.07}$	0.44	$0.70^{+0.10}_{-0.05}$	0.40	$0.39^{+0.05}_{-0.04}$	792/909	783 ± 41
r8	$0.15^{+0.02}_{-0.02}$	$0.82^{+0.09}_{-0.05}$	$1.60^{+0.30}_{-0.37}$	$2.71^{+0.30}_{-0.39}$	0.46	0.59	0.44	0.52	$0.66^{+0.24}_{-0.20}$	$0.34^{+0.06}_{-0.04}$	883/910	778 ± 42
r9	$0.18^{+0.03}_{-0.03}$	$0.70^{+0.03}_{-0.04}$	$1.67^{+0.33}_{-0.26}$	$1.63^{+0.12}_{-0.85}$	0.46	0.59	0.44	$0.71^{+0.15}_{-0.14}$	0.40	0.29	760/911	741 ± 41
r10*	$0.27^{+0.02}_{-0.03}$	$0.93^{+0.02}_{-0.01}$	$2.61^{+0.27}_{-0.40}$	$7.20^{+0.22}_{-0.25}$	0.46	$0.51^{+0.03}_{-0.03}$	0.44	0.52	0.40	0.29	967/911	855 ± 42
r11	$0.10^{+0.02}_{-0.02}$	$1.04^{+0.12}_{-0.07}$	$1.61^{+0.46}_{-0.27}$	$1.61^{+0.22}_{-0.13}$	$0.56^{+0.09}_{-0.08}$	0.59	$0.51^{+0.08}_{-0.07}$	0.52	0.40	$0.40^{+0.04}_{-0.06}$	872/909	779 ± 41
r12	$0.12^{+0.02}_{-0.03}$	$0.97^{+0.04}_{-0.03}$	$1.88^{+0.26}_{-0.23}$	$1.82^{+0.07}_{-0.08}$	0.46	0.59	0.44	$0.63^{+0.10}_{-0.10}$	0.40	0.29	822/911	797 ± 42
r13	$0.11^{+0.02}_{-0.02}$	$1.02^{+0.07}_{-0.07}$	$0.99^{+0.36}_{-0.23}$	$1.25^{+0.09}_{-0.20}$	0.46	0.59	$0.38^{+0.06}_{-0.06}$	0.52	0.40	0.29	849/911	784 ± 40
r14	$0.05^{+0.01}_{-0.01}$	$0.77^{+0.04}_{-0.05}$	$1.42^{+0.31}_{-0.25}$	$4.05^{+0.15}_{-0.14}$	$0.29^{+0.04}_{-0.03}$	$0.43^{+0.03}_{-0.03}$	$0.37^{+0.04}_{-0.04}$	$0.36^{+0.07}_{-0.04}$	0.40	0.29	827/908	789 ± 41
r15	$0.10^{+0.02}_{-0.02}$	$0.95^{+0.10}_{-0.08}$	$1.03^{+0.31}_{-0.23}$	$1.00^{+0.15}_{-0.14}$	0.46	0.59	$0.38^{+0.08}_{-0.08}$	$0.33^{+0.12}_{-0.11}$	0.40	$0.44^{+0.08}_{-0.07}$	789/909	758 ± 40
r16	$0.02^{+0.02}_{-0.01}$	$0.79^{+0.04}_{-0.03}$	$1.47^{+0.16}_{-0.27}$	$3.11^{+0.32}_{-0.27}$	0.46	$0.69^{+0.04}_{-0.03}$	0.44	0.52	$0.86^{+0.26}_{-0.23}$	0.29	827/910	786 ± 41
r17	$0.07^{+0.02}_{-0.02}$	$1.04^{+0.08}_{-0.07}$	$0.96^{+0.20}_{-0.18}$	$0.81^{+0.07}_{-0.06}$	0.46	$0.73^{+0.07}_{-0.06}$	0.44	0.52	$1.84^{+0.56}_{-0.47}$	0.29	767/910	766 ± 41
r18	$0.02^{+0.01}_{-0.01}$	$0.76^{+0.03}_{-0.02}$	$2.26^{+0.24}_{-0.22}$	$5.84^{+0.34}_{-0.35}$	0.46	$0.45^{+0.03}_{-0.03}$	0.44	0.52	0.40	$0.36^{+0.03}_{-0.02}$	883/910	804 ± 42
r19	$0.02^{+0.01}_{-0.01}$	$0.71^{+0.02}_{-0.01}$	$5.48^{+0.64}_{-0.58}$	$2.46^{+0.07}_{-0.08}$	0.46	$0.69^{+0.06}_{-0.06}$	0.44	0.52	0.40	0.29	800/911	758 ± 41
b1	$0.10^{+0.03}_{-0.02}$	$0.86^{+0.09}_{-0.08}$	$1.59^{+0.86}_{-0.50}$	$0.63^{+0.13}_{-0.10}$	$0.83^{+0.45}_{-0.24}$	0.59	0.48	0.58	0.73	$0.53^{+0.15}_{-0.12}$	770/910	730 ± 39
b2	$0.22^{+0.03}_{-0.03}$	$1.12^{+0.08}_{-0.10}$	$0.95^{+0.30}_{-0.15}$	$0.88^{+0.07}_{-0.05}$	0.46	0.59	0.44	0.52	0.40	0.29	848/912	797 ± 40

Note. See Figure 1 for the location of each region. The abundances are with respect to the Wilms scale (Wilms et al. 2000). Errors are the 68% confidence intervals, equivalent to Gaussian 1σ around the quoted abundance. Columns 2–5 describe the LMC hydrogen column density, electron temperature, ionization timescale, and normalization parameter, respectively. Columns 6–11 describe the best-fit abundances of each element. Column 12 lists cstat(O), which is the observed C-statistic we obtain from Xspec; cstat(E) listed in column 13 is the expected C-statistic from the Kaastra (2017) formulation. The fits are considered unsuccessful if |cstat(O) − cstat(E)| > 2.6σ_E where σ_E^2 is the expected variance of cstat(E). Regions with an asterisk (r3 and r10) are those that could not be fit with a single vpshock model; they were refit with a more complex model as described in Table 5. In region r11, the best fit shows an enhanced abundance of N (which is otherwise tied to O): $N = 0.80 \pm 0.11$. The mean values derived from fitting all of the abundances in all of the regions are presented in Table 6. Spectral fits for all regions are presented in Appendix C.

Table 5
Fit Results of vpshock+vnei Model on Rim Regions Where the Single vpshock Did Not Yield an Acceptable Fit and on Region e1

Region ID (1)	N_H (2)	kT_e (3)	τ (4)	norm (5)	kT_e (6)	τ (7)	norm (8)	O (9)	Ne (10)	Mg (11)	Si (12)	S (13)	Fe (14)	cstat(O)/ dof (15)	cstat(E) $\pm \sigma_E$ (16)
...	10^{22} cm^{-2}	keV	10^{11} cm^{-3} s	10^{-4} cm^{-5}	keV	10^{11} cm^{-3} s	10^{-4} cm^{-5}	...	...	...	...	...	...	...	...
r3	$0.10^{+0.02}_{-0.02}$	$0.64^{+0.02}_{-0.03}$	$6.14^{+2.39}_{-1.48}$	$6.41^{+0.52}_{-0.74}$	$1.64^{+0.59}_{-0.47}$	$0.05^{+0.03}_{-0.02}$	$0.56^{+0.32}_{-0.19}$	0.46	0.59	$0.48^{+0.06}_{-0.06}$	$0.57^{+0.13}_{-0.12}$	0.40	0.29	888/907	829 ± 42
r10	$0.24^{+0.03}_{-0.03}$	$0.76^{+0.08}_{-0.06}$	$3.21^{+0.85}_{-0.61}$	$5.78^{+1.36}_{-0.94}$	$1.54^{+0.67}_{-0.33}$	$0.69^{+0.30}_{-0.21}$	$1.55^{+0.90}_{-0.85}$	0.46	0.59	0.44	0.52	0.40	0.29	943/909	878 ± 43
e1	$0.09^{+0.02}_{-0.01}$	$0.61^{+0.35}_{-0.09}$	$0.70^{+0.20}_{-0.20}$	$1.47^{+0.32}_{-0.19}$	$2.02^{+1.29}_{-0.68}$	$0.42^{+0.38}_{-0.08}$	$0.25^{+0.07}_{-0.16}$	$1.63^{+0.64}_{-0.29}$	$1.59^{+1.00}_{-0.42}$	$2.50^{+1.27}_{-0.35}$	$1.70^{+0.86}_{-0.21}$	0.40	$0.96^{+0.47}_{-0.37}$	858/904	803 ± 41

Note. The spectral fits for the rim regions are presented in Appendix C and for region e1 in Figure 7. Parameters in columns 3–5 consist of the vpshock component, and those in columns 6–14 belong to the vpshock component. Elemental abundances of vpshock are frozen to local LMC averages.
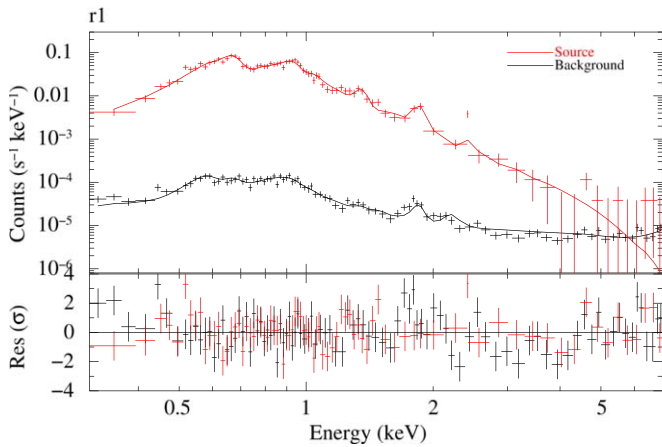
Figure 4. Spectral fit for region r1 on the rim with the single `vpshock` model. Also plotted is the background model fit that shows that the background is significantly less than the source spectrum below 5.5 keV. Note that the data have been rebinned for plotting purposes. All other spectral fits for the rim regions and the blobs are presented in Appendix C.

Table 6
Mean (μ) Local LMC Parameters Obtained from the Fits to the Rim Regions

Parameter	Units	$\mu \pm \sigma_\mu$	Scatter
$N_{\rm H}$	10^{22} cm^{-2}	0.10 ± 0.07	2.74
$kT_{\rm e}$	keV	0.86 ± 0.16	1.37
τ	10^{11} cm^{-3} s	1.94 ± 1.09	1.26
O	⋯	0.50 ± 0.22	1.00
Ne	⋯	0.59 ± 0.16	1.01
Mg	⋯	0.48 ± 0.17	0.93
Si	⋯	0.58 ± 0.24	1.14
S	⋯	0.73 ± 0.52	1.18
Fe	⋯	0.34 ± 0.12	0.96
norm	10^{-4} cm^{-5}	2.69 ± 1.88	4.10

Note. Error (σ_μ) denotes the statistical as well as systematic uncertainty on the mean. Abundances are quoted with respect to the `Wilms` scale. Uniformity of a parameter over the shell is judged by its scatter value. Both σ_μ and scatter are calculated from the method of multiple imputations (see Appendix B).

SNR G292.0 + 1.8 and Cas A, where the optical emission is proposed to come from dense ejecta-rich knots and the X-ray emission from a lower density plasma (Ghavamian et al. 2005; Patnaude & Fesen 2014).

4.2.2. Regions with Fe K Emission

We use a `vnei + vnei + vpshock` model (referred to as the *ionizing* model) to fit the spectra in regions f1–f6. We also use a *recombining* plasma model (`vrnei + vnei + vpshock`) as an alternate explanation to look for possible signatures of a recombining plasma in N132D. These models contain three components: one to account for shell emission along the line of sight (`vpshock`), a second to account for the cooler soft X-ray emission and some of the high-energy continuum (`vnei2` and `vnei` in the ionizing and recombining models, respectively), and a third to account for the hotter Fe K emission and the remainder of the hard X-ray spectra (`vnei1` and `vrnei` in the ionizing and recombining models, respectively). We find that a three-component fit is essential because no combination of a two-component model of an NEI plasma is able to model the Fe K feature while simultaneously explaining the Fe L shell emission around 1 keV. Evidence for

the need for a third, hotter component is established when we artificially increase the abundance of Fe in the NEI component of a two-component (`vnei/vrnei + vpshock`) model to reproduce the observed flux in the Fe K feature. This experiment of increasing the Fe abundance in order to get enough flux in the Fe Kα line overproduces the Fe L emission at ∼1 keV. Thus, we establish that at least two separate plasma conditions are needed to explain the Fe L (∼1 keV) and Fe K (∼6.7 keV) emissions, which has been noted before for this remnant (Maggi et al. 2016; Bamba et al. 2018).

We show the best-fit parameters for the ionizing and recombining models for regions f1–f6 in Table 7 and the corresponding spectral plots in Figures 8 and C11–C15, respectively. Note that the total emission (top black histogram and curve) includes the background model, which is why it levels off at a higher level than the magenta curves in the inset in these figures. Several features of these fits should be highlighted. First, the quality of the fit in terms of the fit statistic `cstat(O)/dof` is indistinguishable for the *ionizing* and *recombining* plasma models in all of the regions. Based on these results, we cannot conclude that one model is preferred over the other. We also note that the initial electron temperature (`kT_init`) for the `vrnei` component in the recombining models is highly degenerate and gives similar results for temperatures higher than 10 keV (see also Bamba et al. 2018); hence, we freeze it at this value (see, for example, Auchettl et al. 2017; Katsuragawa et al. 2018). Further, we find that both of the model fits for regions f1, f2, f4, and f6 are acceptable according to our criteria, whereas those for regions f3 and f5 are marginally inconsistent with our chosen acceptability criteria because for the latter two `cstat (O)` ≈ `cstat (E)` + $3.1\sigma_{\rm E}$. This indicates that overall the fits are good, but there are details that the models fail to reproduce. It also highlights the trade-off between using large regions that encompass sufficient Fe K emission and the existence of multiple plasma conditions within them that complicate the spectral modeling.

The electron temperatures and ionization timescales for the shell and the cooler X-ray emission model components are identical in both of the models in all six regions; they fall into the partial nonequilibration category as defined by Vink (2012, see their Section 5.3). Additionally, both the best-fit ionizing and recombining plasma models result in abundances for Si and Fe (in the hotter component) that are significantly enhanced compared to the expected abundances for the LMC in four out of the six regions. The enhanced abundance of Fe in these regions distinguishes them from the regions at the rim. The regions interior to the remnant contain plasma with a sufficiently high temperature and Fe abundance to produce the observed Fe K emission. We also let the abundances of O, Ne, and Mg vary and find that both of the best-fit models have enriched Ne and Mg in the cooler model component in regions f1 and f6 and in the recombining plasma model in region f3.

Although there are several similarities in the two models that lead us to conclude they cannot be distinguished with the current data, there are subtle differences that provide some understanding of the plasma conditions in these regions. For example, `cstat(O)` is slightly less for the recombining plasma models in regions f1, f2, f3, and f6. The ionization timescale for the hotter NEI component in the ionizing model (`vnei1`) approaches equilibrium within the uncertainties in regions f3, f4, and f6, whereas that for the recombining model
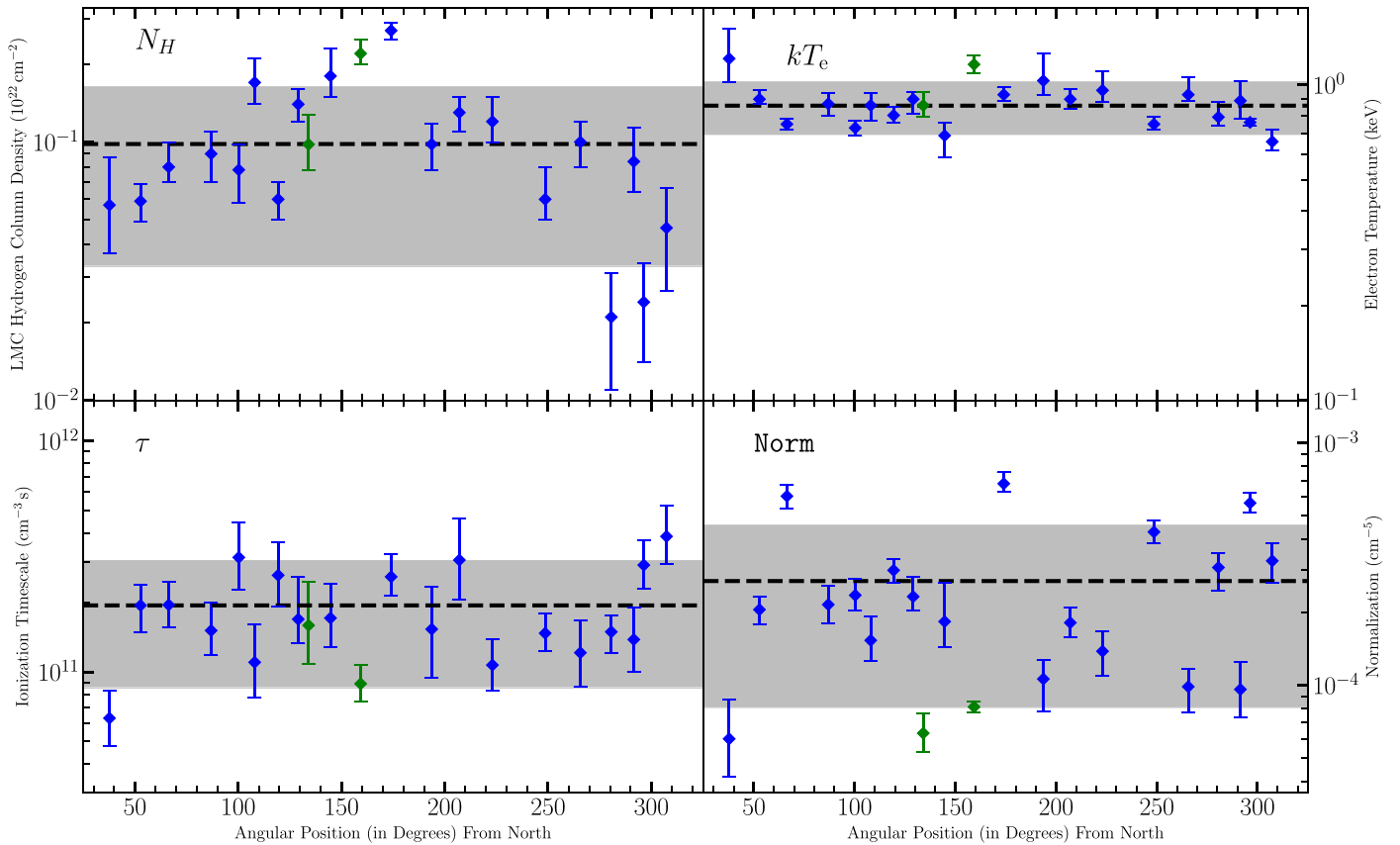
Figure 5. Trends along the rim for a plane-parallel shock model (`vpshock`). The horizontal axis depicts the angular position of each region (in degrees) clockwise from the north. Blue markers denote values for the rim regions, and green markers denote values for the blobs (see Figure 1 for information on the location of each region). The dashed line depicts the mean local LMC value for each parameter (see Table 6), and the shaded area corresponds to the total (statistical+systematic) uncertainty on the mean.

essentially represents a nonequilibrium plasma (except perhaps for region f6). This could imply that the plasma is in fact evolving through recombination post equilibrium. The recombining models also exhibit a typical LMC abundance of S in the `vrnei` component, except for region f4. The constraints on best-fit abundances are tighter in the recombining models, and there are no values that might be nonphysical and simply a result of the complex nature of the fit, such as the abundance of Si in the hotter model component in region f2 in the ionizing model, which is $\sim 7\times$ the solar value. The hottest plasma component in the recombining model contributes more to the emission at lower energies than the ionizing model, while both components explain the Fe K emission. A similar observation can also be made by realizing that the emission measure (`norm`) of the hotter component in the recombining model is larger than that in the corresponding ionizing model, except for region f6. This hints at the possibility of different origins of the hot plasma in different parts of the remnant, as has been shown for the SNR G290.1-0.8 (Kamitsukasa et al. 2015), as well as in simulations of an SNR shock interacting with a distribution of clouds in the ISM (Zhang et al. 2019), but no definitive conclusions on the origin of the hot component can be drawn from the current data.[6]

Thus, we establish from this analysis that (1) Fe K emission in N132D is not contained in a single ejecta clump or discrete

feature, rather, it is largely spread across the southern half of the remnant, and (2) the plasma that leads to the production of Fe K is either hot with a surprisingly large value of the ionization timescale or undergoing recombination (with slight indications in favor of the latter). In either case, this plasma is physically distinct from the plasma that produces the soft X-ray emission. We further discuss its implications in Section 5.4.

5. Discussion

5.1. LMC Abundances and Their Variations

Analysis of the rim regions provides a means to estimate the LMC abundances local to N132D that can inform us about the metallicity of the circumstellar medium (CSM) prior to the explosion. Table 8 shows the mean abundances for the elements we include in this study, along with measurements from previous works. Before we can meaningfully compare these abundances, it is important to remark on several characteristics that influence these measurements and should be kept in mind. The first row of Table 8 lists the number of regions used by different authors to determine the mean local abundances; "W" denotes that certain studies derived the mean abundances from fits to the integrated spectrum of the whole remnant. Further, note that some studies used a combination of regions on the rim and the interior of the remnant; two out of eight regions used by Schenck et al. (2016) and two out of the four regions used by Dopita et al. (2018) are in the interior. For the results from Dopita et al. (2018) and Korn et al. (2002) that

---

[6] Note that both Kamitsukasa et al. (2015) and Zhang et al. (2019) work with mixed-morphology remnants, whereas N132D has not been classified as one so far.
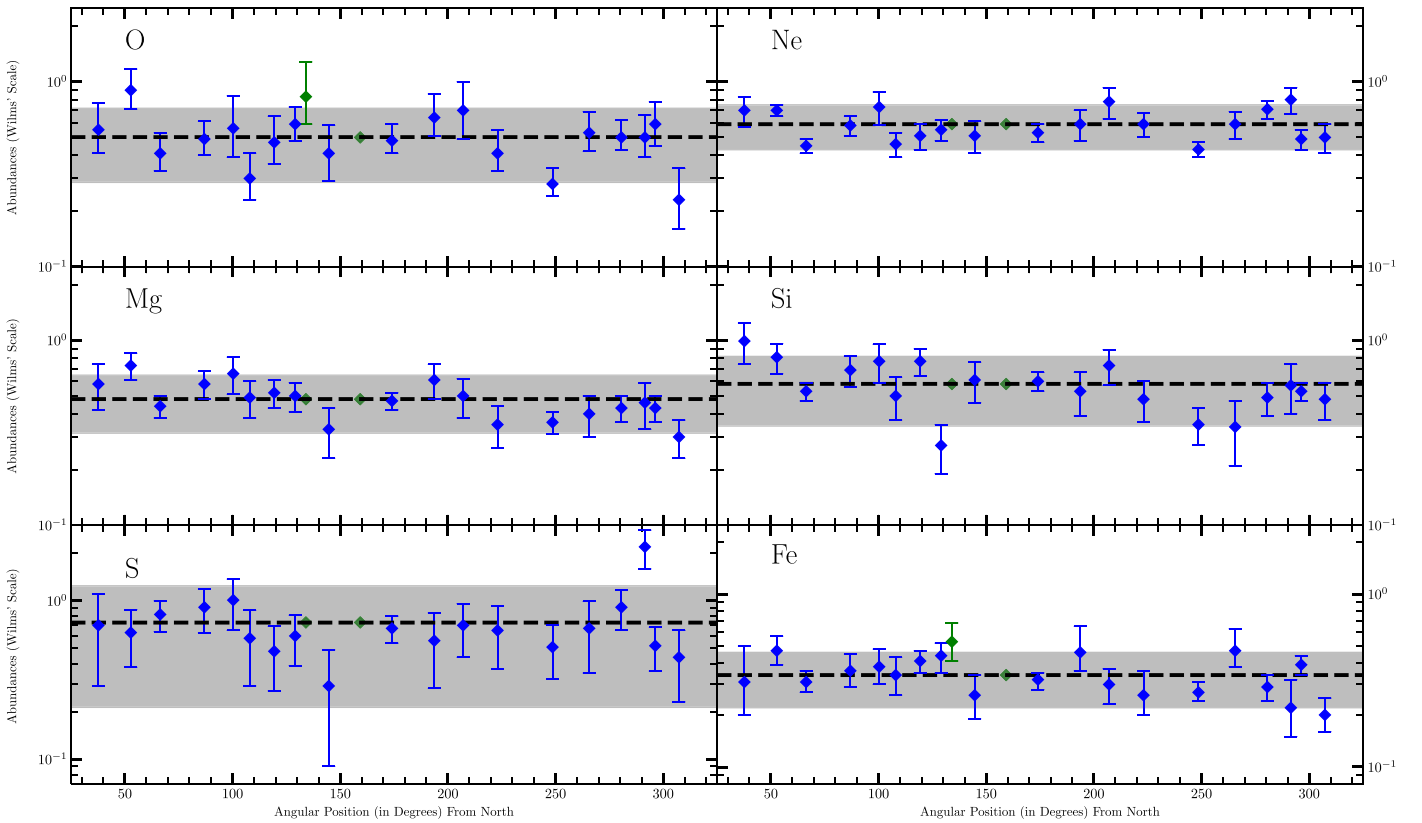
Figure 6. Same as Figure 5, showing abundance pattern across the rim. The vertical axis is the abundance value relative to cosmic on the Wilms et al. (2000) scale. Blue markers denote values for the rim regions, and green markers denote values for the blobs. The shaded area depicts the $\mu \pm \sigma_\mu$ domain for each abundance, where μ is the average value local to N132D (denoted by dashed lines) and σ_μ is the total (statistical+systematic) uncertainty on the mean that we use as a criteria to classify an abundance as enhanced or reduced (see Appendix B). The mean local LMC value (μ) for each parameter is available in Table 6, along with a comparison with other works in Table 8.
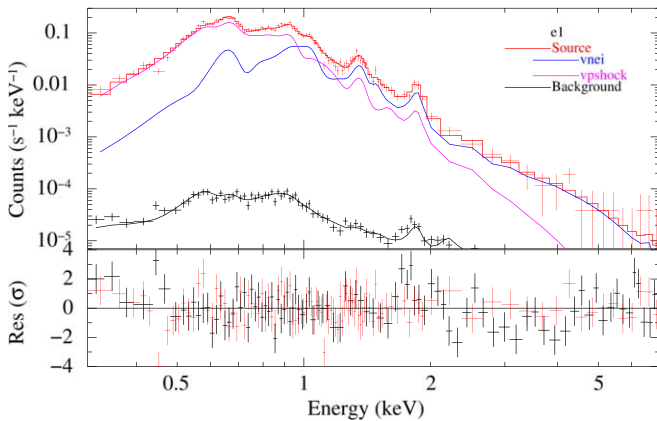
Figure 7. Fit and residuals for region e1 with the (vpshock + vnei) model. The best-fit parameters are listed in Table 5. This region shows enhanced abundances ($\gtrsim 2.5\times$ mean) of all elements (except S) and contains one or more X-ray-bright ejecta fragments. It partially overlaps with the ejecta fragment seen in the optical (Morse et al. 1996, 1995; Blair et al. 2000) as shown in Figure 1. Also plotted is the background, which is significantly less than the source at energies <5.5 keV. Note that the spectral counts have been rebinned for display purposes.

are derived from observations with the ANU Wide-Field Spectrograph (WiFeS; Dopita et al. 2010), we average over the four brightest clouds (in the optical) that were used to determine the abundances. There is no uncertainty on the abundance of Mg local to N132D because it could not be constrained from the data used and was fixed to one-half of the

solar value. For Fe, spectral fits to the four brightest clouds returned the same value. The measurements from Dopita et al. (2019) are from the same regions as in Dopita et al. (2018), but with an improved shock modeling code that takes into account the emission from the photoionization region ahead of the forward shock. The quoted abundances of Mg, Si, and Fe from Dopita et al. (2019) are the values assumed by the authors in the model.

The values in parentheses that we quote from Hughes et al. (1998) and Schenck et al. (2016) represent abundances averaged over multiple SNRs in the LMC, the ones we take from Russell & Dopita (1992) are averaged over SNRs as well as supergiants, and those from Dopita et al. (2018) and Korn et al. (2002) are determined from N132D and B-stars in NGC 2004. The ones we report from Dopita et al. (2019) in parentheses are averaged over SNRs, B-stars, F-supergiants, and H II regions. Different studies have also used different observations to compute the mean abundances local to N132D, as we show in Table 8. The effect of dust depletion is only accounted for by Dopita et al. (2018) and Dopita et al. (2019), although the effects of depletion in different phases and shock conditions are largely unknown (see, for example, Williams et al. 2006; Maggi et al. 2019). For our work, we find the error and scatter of the fitted abundances using the method of Multiple Imputations (Lee et al. 2011), which takes into account the statistical and systematic uncertainties on the parameters (see Appendix B for further details). We suspect that the abundance of S is not well constrained because of the

Table 7
Ionizing and Recombining Plasma Model Fits for Regions That Have a Weak Signature of Fe K Emission (See Figures 8 and C11–C15)

Ionizing Model Parameter	Units	Region f1	Region f2	Region f3	Region f4	Region f5	Region f6	Recombining Model Parameter	Units	Region f1	Region f2	Region f3	Region f4	Region f5	Region f6
N_H	10^{22} cm^{-2}	$0.09^{+0.01}_{-0.01}$	$0.16^{+0.01}_{-0.01}$	$0.16^{+0.01}_{-0.01}$	$0.14^{+0.01}_{-0.01}$	$0.18^{+0.01}_{-0.01}$	$0.15^{+0.01}_{-0.01}$	N_H	10^{22} cm^{-2}	$0.09^{+0.01}_{-0.01}$	$0.15^{+0.01}_{-0.01}$	$0.16^{+0.01}_{-0.01}$	$0.15^{+0.01}_{-0.01}$	$0.18^{+0.01}_{-0.01}$	$0.15^{+0.01}_{-0.01}$
kT_evnei 1	keV	$2.66^{+0.32}_{-0.29}$	$2.70^{+0.11}_{-0.14}$	$1.88^{+0.11}_{-0.13}$	$2.43^{+0.14}_{-0.32}$	$1.75^{+0.03}_{-0.14}$	$1.45^{+0.06}_{-0.04}$	kT_evrnei	keV	$1.97^{+0.21}_{-0.21}$	$1.33^{+0.16}_{-0.17}$	$1.27^{+0.08}_{-0.07}$	$2.06^{+0.45}_{-0.39}$	$1.54^{+0.19}_{-0.13}$	$1.45^{+0.04}_{-0.07}$
...	...	...	...	...	...	...	...	kT_init vrnei	keV	10	10	10	10	10	10
Si	...	$3.27^{+2.41}_{-1.14}$	$6.95^{+3.45}_{-0.76}$	$1.67^{+0.68}_{-0.27}$	$2.30^{+1.76}_{-0.79}$	$1.75^{+0.56}_{-0.45}$	$1.02^{+0.16}_{-0.15}$	Si	...	$3.17^{+0.94}_{-0.82}$	$2.64^{+1.42}_{-0.95}$	$0.91^{+0.16}_{-0.10}$	$3.05^{+1.64}_{-0.88}$	$1.71^{+0.29}_{-0.34}$	$1.03^{+0.18}_{-0.14}$
S	...	$1.69^{+0.81}_{-0.62}$	$1.50^{+0.69}_{-0.42}$	$0.73^{+0.29}_{-0.23}$	$1.56^{+0.92}_{-0.65}$	$0.79^{+0.43}_{-0.35}$	$0.73^{+0.15}_{-0.14}$	S	...	$1.66^{+0.80}_{-0.66}$	$0.39^{+0.64}_{-0.04}$	$0.39^{+0.15}_{-0.15}$	$2.72^{+1.49}_{-0.86}$	$0.91^{+0.30}_{-0.28}$	$0.56^{+0.17}_{-0.16}$
Fe	...	$2.59^{+0.79}_{-0.70}$	$1.87^{+0.37}_{-0.27}$	$0.90^{+0.17}_{-0.15}$	$1.37^{+0.57}_{-0.33}$	$0.61^{+0.15}_{-0.18}$	$0.47^{+0.07}_{-0.11}$	Fe	...	$2.11^{+0.50}_{-0.42}$	$0.78^{+0.38}_{-0.29}$	$0.49^{+0.13}_{-0.06}$	$1.67^{+0.72}_{-0.19}$	$0.56^{+0.13}_{-0.12}$	$0.43^{+0.06}_{-0.07}$
τ vnei1	10^{11} cm^{-3} s	$4.84^{+1.54}_{-1.19}$	$5.91^{+3.66}_{-1.94}$	$7.11^{+5.93}_{-1.94}$	$6.21^{+10.58}_{-2.74}$	$5.50^{+3.14}_{-1.52}$	$6.27^{+5.13}_{-2.64}$	τ vrnei	10^{11} cm^{-3} s	$5.93^{+6.40}_{-2.12}$	$2.20^{+0.45}_{-0.49}$	$4.52^{+0.64}_{-0.44}$	$4.97^{+5.34}_{-2.09}$	$6.43^{+3.25}_{-2.15}$	$7.71^{+3.01}_{-1.04}$
norm vnei 1	10^{-4} cm^{-5}	$1.67^{+0.37}_{-0.26}$	$2.25^{+0.51}_{-0.49}$	$12.44^{+2.03}_{-1.12}$	$2.73^{+0.93}_{-0.93}$	$7.49^{+1.36}_{-1.01}$	$16.49^{+1.42}_{-1.62}$	norm vrnei	10^{-4} cm^{-5}	$2.73^{+0.34}_{-0.30}$	$8.60^{+3.83}_{-3.16}$	$34.31^{+8.59}_{-5.09}$	$2.84^{+1.28}_{-0.52}$	$9.33^{+1.88}_{-1.38}$	$13.48^{+1.86}_{-1.23}$
kT_evnei 2	keV	$1.04^{+0.03}_{-0.04}$	$0.74^{+0.01}_{-0.01}$	$0.92^{+0.02}_{-0.03}$	$0.89^{+0.04}_{-0.03}$	$0.87^{+0.04}_{-0.03}$	$0.88^{+0.02}_{-0.02}$	kT_evnei	keV	$1.02^{+0.03}_{-0.02}$	$0.74^{+0.02}_{-0.01}$	$0.90^{+0.04}_{-0.03}$	$0.89^{+0.04}_{-0.03}$	$0.86^{+0.03}_{-0.03}$	$0.89^{+0.04}_{-0.03}$
Ne	...	$1.65^{+0.69}_{-0.75}$	$0.87^{+0.10}_{-0.06}$	$0.89^{+0.15}_{-0.13}$	$0.77^{+0.14}_{-0.13}$	$0.83^{+0.18}_{-0.08}$	$1.31^{+0.22}_{-0.20}$	Ne	...	$1.91^{+0.85}_{-0.60}$	$1.00^{+0.24}_{-0.12}$	$1.40^{+1.65}_{-0.28}$	$0.74^{+0.09}_{-0.24}$	$0.83^{+0.08}_{-0.09}$	$1.36^{+0.14}_{-0.24}$
Mg	...	$0.98^{+0.26}_{-0.27}$	$0.71^{+0.06}_{-0.02}$	$0.68^{+0.06}_{-0.07}$	$0.58^{+0.10}_{-0.04}$	$0.70^{+0.07}_{-0.08}$	$0.98^{+0.08}_{-0.10}$	Mg	...	$1.15^{+0.25}_{-0.30}$	$0.90^{+0.23}_{-0.12}$	$1.21^{+2.27}_{-0.30}$	$0.54^{+0.04}_{-0.02}$	$0.71^{+0.05}_{-0.13}$	$0.99^{+0.23}_{-0.13}$
Si	...	$0.85^{+0.25}_{-0.16}$	$0.64^{+0.05}_{-0.03}$	$0.71^{+0.07}_{-0.06}$	$0.60^{+0.09}_{-0.08}$	$0.64^{+0.05}_{-0.09}$	$0.82^{+0.13}_{-0.04}$	Si	...	$0.98^{+0.12}_{-0.10}$	$0.81^{+0.21}_{-0.11}$	$1.41^{+4.32}_{-0.43}$	$0.57^{+0.10}_{-0.09}$	$0.67^{+0.06}_{-0.11}$	$0.88^{+0.09}_{-0.13}$
S	...	$0.52^{+0.22}_{-0.17}$	$0.68^{+0.09}_{-0.07}$	$0.65^{+0.11}_{-0.11}$	$0.47^{+0.09}_{-0.10}$	$0.47^{+0.14}_{-0.09}$	$0.62^{+0.37}_{-0.30}$	S	...	$0.67^{+0.18}_{-0.17}$	$0.94^{+0.10}_{-0.13}$	$1.52^{+0.47}_{-0.30}$	$0.49^{+0.12}_{-0.05}$	$0.54^{+0.13}_{-0.08}$	$0.97^{+0.11}_{-0.16}$
Fe	...	$0.45^{+0.10}_{-0.06}$	$0.37^{+0.02}_{-0.01}$	$0.38^{+0.03}_{-0.03}$	$0.34^{+0.04}_{-0.03}$	$0.40^{+0.06}_{-0.04}$	$0.41^{+0.07}_{-0.03}$	Fe	...	$0.51^{+0.04}_{-0.04}$	$0.50^{+0.08}_{-0.07}$	$0.76^{+3.64}_{-0.05}$	$0.32^{+0.05}_{-0.05}$	$0.42^{+0.02}_{-0.04}$	$0.55^{+0.11}_{-0.06}$
τ vnei2	10^{11} cm^{-3} s	$3.47^{+0.35}_{-0.30}$	$3.78^{+0.27}_{-0.25}$	$2.51^{+0.28}_{-0.14}$	$2.19^{+0.39}_{-0.32}$	$2.88^{+0.31}_{-0.37}$	$2.7^{+0.19}_{-0.17}$	τ vnei	10^{11} cm^{-3} s	$3.49^{+1.11}_{-0.70}$	$3.39^{+0.37}_{-0.33}$	$2.10^{+0.24}_{-0.26}$	$2.16^{+0.40}_{-0.29}$	$2.79^{+0.11}_{-0.11}$	$2.88^{+0.43}_{-0.36}$
norm vnei 2	10^{-4} cm^{-5}	$8.16^{+0.73}_{-0.33}$	$34.72^{+1.61}_{-0.49}$	$40.16^{+3.22}_{-2.64}$	$20.04^{+2.74}_{-2.51}$	$22.63^{+3.79}_{-4.10}$	$18.21^{+1.08}_{-0.49}$	norm vnei	10^{-4} cm^{-5}	$7.14^{+0.30}_{-0.45}$	$25.64^{+4.48}_{-4.79}$	$18.43^{+8.17}_{-10.22}$	$21.31^{+0.59}_{-2.21}$	$21.57^{+2.22}_{-2.05}$	$18.63^{+3.26}_{-2.88}$
kT_evpshock	keV	$0.59^{+0.03}_{-0.04}$	$0.38^{+0.02}_{-0.07}$	$0.49^{+0.03}_{-0.03}$	$0.47^{+0.04}_{-0.06}$	$0.53^{+0.05}_{-0.05}$	$0.51^{+0.05}_{-0.04}$	kT_evpshock	keV	$0.59^{+0.01}_{-0.01}$	$0.38^{+0.03}_{-0.08}$	$0.49^{+0.04}_{-0.06}$	$0.45^{+0.05}_{-0.03}$	$0.52^{+0.05}_{-0.06}$	$0.52^{+0.06}_{-0.03}$
τ vpshock	10^{11} cm^{-3} s	$4.14^{+0.26}_{-0.26}$	$6.33^{+2.97}_{-1.22}$	$4.90^{+0.55}_{-0.42}$	$4.75^{+1.46}_{-0.62}$	$5.27^{+0.38}_{-0.38}$	$3.10^{+1.36}_{-0.36}$	τ vpshock	10^{11} cm^{-3} s	$4.09^{+1.04}_{-0.25}$	$6.37^{+1.90}_{-1.69}$	$4.85^{+1.04}_{-0.79}$	$4.98^{+1.50}_{-1.22}$	$5.26^{+0.77}_{-0.59}$	$3.29^{+0.57}_{-0.43}$
norm vpshock	10^{-4} cm^{-5}	$12.09^{+0.40}_{-0.67}$	$21.10^{+4.31}_{-2.47}$	$31.76^{+1.36}_{-1.46}$	$23.88^{+1.56}_{-0.78}$	$19.63^{+1.72}_{-2.90}$	$16.20^{+1.69}_{-0.78}$	norm vpshock	10^{-4} cm^{-5}	$11.72^{+0.73}_{-0.69}$	$21.74^{+2.36}_{-1.40}$	$31.16^{+1.94}_{-1.81}$	$23.65^{+1.61}_{-1.69}$	$19.18^{+2.48}_{-1.87}$	$17.02^{+1.76}_{-1.40}$
cstat(O)/dof	...	1126/966	1048/966	1190/966	1110/966	1173/966	1135/966	cstat(O)/dof	...	1110/966	1042/966	1182/966	1110/966	1171/966	1126/966
cstat(E) $\pm \sigma_\mathrm{E}$	...	1018 ± 45	1018 ± 46	1039 ± 49	1017 ± 45	1025 ± 48	1018 ± 45	cstat(E) $\pm \sigma_\mathrm{E}$	...	1021 ± 45	1010 ± 46	1038 ± 47	1017 ± 45	1025 ± 47	1014 ± 45

Note. Elemental abundances of respective model components not shown here are all frozen to average local LMC values (as in Table 6).
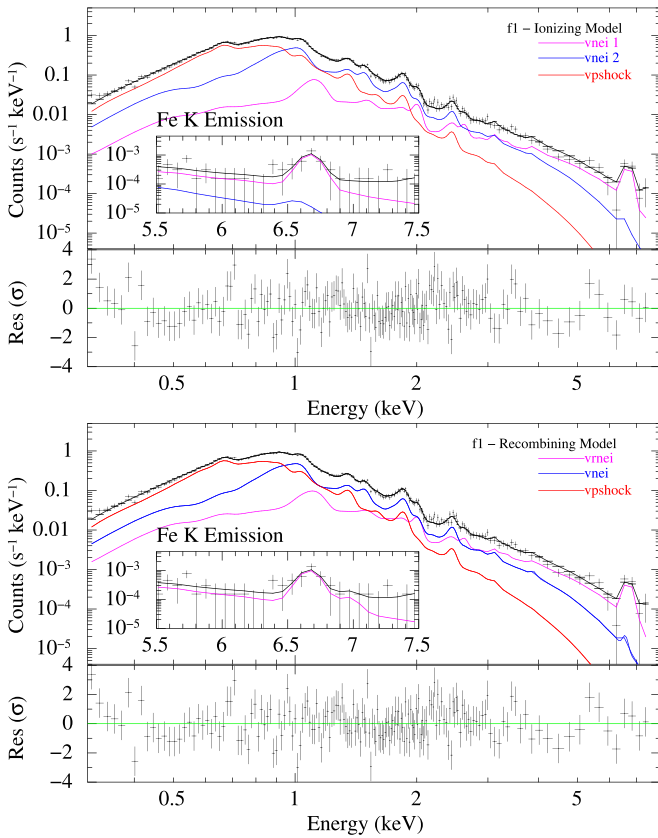
Figure 8. Fits and residuals for the region f1, showing the weak Fe K emission feature present at ~6.7 keV. The inset zooms into the energy range 5.5–7.5 keV that contains this emission. The fit parameters for both the ionizing and recombining models are presented in Table 7. With the current number of counts, it is difficult to distinguish between the origin and the nature of the plasma since the spectral fits of both models are statistically the same. Note that the spectral counts have been rebinned differently in the main plot and in the inset for display purposes. Spectral plots for other Fe K regions are presented in Appendix C.

low number of S counts on the rim; this is also apparent in its relatively large 1σ uncertainty.

Our measurements that are local to N132D match closely with Blair et al. (2000), except for Mg and S. However, the abundance of Mg reported in Blair et al. (2000) is classified as a lower limit by the authors, whereas that of S is within the uncertainty. Our measurements of Ne and Mg are higher and lower, respectively, than the measurements of Dopita et al. (2018) and Korn et al. (2002), but they are in good agreement with those of Dopita et al. (2019). As compared to Maggi et al. (2016), we measure consistent (within the uncertainties) abundances of Ne, Si, and Fe. There is a significant discrepancy of ~1.0 dex between the abundance of O measured by Maggi et al. (2016) and other works including ours. We note that we have adopted the best-fit abundance values for the CSM/ISM model component for N132D from Table E.2 of Maggi et al. (2016), whereas the majority of the O emission is fitted by the hotter, O-rich model component in their model.

Similarly, we can compare our results with that of Schenck et al. (2016), especially because the same archival Chandra data have been used in both studies. It is worth noting that our measurements of the abundances of O, Ne, and Mg are 0.4 dex higher, whereas those of Si and Fe are in excellent agreement with that of Schenck et al. (2016). We speculate that the reason for this discrepancy can be that our measurements are derived

from fitting the entire rim, whereas those of Schenck et al. (2016) come from fitting certain regions located on different parts of the rim as well as some regions in the interior. In fact, we find that some of the regions on the rim analyzed by Schenck et al. (2016) have systematically lower abundances than the average in our fits to the same regions (regions r13–r15).

5.2. Shock Velocity and Electron Density

We calculate the forward-shock velocity and an estimate of the shock age along the rim using average physical conditions of the plasma (temperature and ionization timescale), the geometry of the region (see Figure D1), and its `norm`. Using the Rankine–Hugoniot conditions, which predict mass-proportional heating for electrons and ions (Landau & Lifshitz 1975; Berezhko & Ellison 1999; Vink 2012), and assuming no energy losses (for example, due to cosmic rays), we can relate the electron temperature to the shock velocity as

$$kT_e \approx \frac{3}{16}m_\mu v_s^2, \tag{1}$$

where m_μ is the mean mass per free particle, and v_s is the shock velocity. Assuming the majority of the electrons are contributed by H and He, $m_\mu \sim 0.59\,m_H$. The mean electron temperature we find from our analysis of the rim regions is $\langle kT_e \rangle = 0.85 \pm 0.20$ keV (see Table 6). Then the mean shock velocity of the blast wave is $\langle v_s \rangle = 855 \pm 100$ km s^{-1}. We estimate the average shock age (by finding the electron density n_e using the `norm` and the 3D geometrical approximation described in Appendix D) to be $\langle \tau \rangle = (1200 \pm 270)f^{-1/2}$ yr for the rim, where f denotes the volume filling factor of the shell region. Filling factor refers to the fraction of emitting plasma filling a volume in the remnant and is a parameter to account for our lack of knowledge about the extent of the emitting volume that is filled with X-ray-emitting plasma (Higdon & Lingenfelter 1980). Table 9 lists the corresponding shock velocities, electron densities, and shock ages we find for all of the rim regions.

Through simulations of a blast wave evolving into a cavity and colliding with clouds, Tang et al. (2016) propose that the shock velocity is decreased by roughly $\sqrt{n_e}$ when the blast wave hits the clouds. For the mean shock velocity $(855 \pm 100$ km s$^{-1})$ and electron density $(6 \pm 2f^{-1/2}$ cm$^{-3})$ we derive, this implies a mean precollision blast wave velocity of ~2100 km s^{-1} (if $f \sim 1$). This is in good agreement with the precollision velocity of 1900 km s^{-1} proposed by Chen et al. (2003) for N132D, where the authors use a semi-analytical thin shell model to study an SNR crossing a density jump (a condition that can prevail in SNRs expanding in a low-density cavity). For N132D, Chen et al. (2003) conclude that the current shock had been interacting with denser material for ~700 yr when it was slowed down to ~700 km s^{-1} from its precollision value by impact with the walls of the cavity in which the massive progenitor is thought to have exploded. Thus, the observations are consistent with a scenario in which this SNR exploded inside a cavity (in a denser surrounding medium) possibly created by the winds of its progenitor.

14

Table 8
Comparison of Mean Abundances Local to N132D with Other Works

Element	Solar (a)	Russell and Dopita (b)	Hughes (c)	Blair (d)	Schenck (e)	Maggi (f)	Dopita/Korn (g)	Dopita19 (h)	This Work
...	...	W	W	1	8	W	4	4	19
...	...	...	ASCA	HST	Chandra	XMM-Newton	WiFeS	WiFeS	Chandra
O	8.69	$[8.35 \pm 0.06]$	8.14 ± 0.06 $[8.21 \pm 0.07]$	8.45 ± 0.10	7.97 ± 0.09 $[8.04 \pm 0.04]$	$7.39^{+0.17}_{-0.09}$ $[8.01^{+0.14}_{-0.21}]$	$8.31^{+0.01}_{-0.03}$ $[8.32 \pm 0.06]$	8.32 ± 0.04 $[8.40 \pm 0.05]$	8.39 ± 0.19
Ne	7.94	$[7.61 \pm 0.05]$	7.56 ± 0.06 $[7.55 \pm 0.08]$	7.64 ± 0.10	7.29 ± 0.06 $[7.39 \pm 0.06]$	7.60 ± 0.02 $[7.39^{+0.11}_{-0.15}]$	$7.44^{+0.01}_{-0.03}$ $[7.52 \pm 0.09]$	7.62 ± 0.04 $[7.70 \pm 0.09]$	7.71 ± 0.12
Mg	7.40	$[7.47 \pm 0.13]$	7.08 ± 0.07 $[7.08 \pm 0.07]$	6.75 ± 0.10	6.73 ± 0.07 $[6.88 \pm 0.06]$	6.68 ± 0.02 $[6.92^{+0.20}_{-0.37}]$	7.47 $[7.37 \pm 0.06]$	7.19 $[7.19 \pm 0.09]$	7.08 ± 0.15
Si	7.27	$[7.81]$	7.08 ± 0.13 $[7.04 \pm 0.08]$	7.00 ± 0.10	7.00 ± 0.07 $[6.99 \pm 0.11]$	6.86 ± 0.03 $[7.11^{+0.20}_{-0.41}]$	$[7.10 \pm 0.07]$	7.11 $[7.11 \pm 0.04]$	7.03 ± 0.18
S	7.09	$[6.70 \pm 0.09]$	6.73 ± 0.06 $[6.71]$	6.63 ± 0.10	...	...	$7.01^{+0.09}_{-0.06}$ $[7.00 \pm 0.15]$	7.10 ± 0.07 $[6.93 \pm 0.05]$	6.95 ± 0.31
Fe	7.43	$[7.23 \pm 0.14]$	7.08 ± 0.06 $[7.01 \pm 0.11]$	6.85 ± 0.10	6.97 ± 0.07 $[6.84 \pm 0.05]$	6.88 ± 0.02 $[6.97^{+0.13}_{-0.18}]$	7.23 $[7.33 \pm 0.03]$	7.33 $[7.33]$	6.96 ± 0.15

Note. Values in parentheses denote those averaged over many SNRs in the LMC. The first row denotes the number of regions within the remnant used for the analysis; "W" denotes that the abundances were derived from the fit to the integrated spectrum of the entire remnant. The second row denotes the instrument or observatory source of the measurements local to N132D.

References. (a) Wilms et al. (2000), (b) Russell & Dopita (1992), (c) Hughes et al. (1998), (d) Blair et al. (2000), (e) Schenck et al. (2016), (f) Maggi et al. (2016), (g) Dopita et al. (2018), Korn et al. (2002), (h) Dopita et al. (2019).

Table 9
Shock Velocity (v_s), Electron Density (n_e), and Shock Age (t) in Rim Regions with 1σ Errors

Region ID	v_s (km s^{-1})	n_e ($f^{-1/2}$ cm^{-3})	t ($f^{-1/2}$ yr)
r1	1029 ± 46	3 ± 1	680 ± 110
r2	893 ± 34	4 ± 1	1490 ± 380
r3	745 ± 17	7 ± 3	2620 ± 1020
r4	843 ± 15	5 ± 1	1130 ± 130
r5	784 ± 11	8 ± 2	1380 ± 160
r6	843 ± 57	7 ± 3	850 ± 300
r7	833 ± 21	7 ± 2	1220 ± 190
r8	774 ± 17	7 ± 1	760 ± 180
r9	779 ± 22	4 ± 3	1300 ± 260
r10	812 ± 43	5 ± 3	1990 ± 530
r11	950 ± 55	5 ± 2	990 ± 280
r12	917 ± 19	4 ± 1	1400 ± 190
r13	941 ± 32	4 ± 1	800 ± 290
r14	817 ± 21	6 ± 1	770 ± 170
r15	908 ± 48	5 ± 2	610 ± 180
r16	828 ± 21	6 ± 2	790 ± 90
r17	950 ± 37	3 ± 1	920 ± 190
r18	812 ± 16	8 ± 2	870 ± 100
r19	785 ± 11	7 ± 1	2400 ± 280

Note. v_s is estimated from Equation (1), and n_e from the norm and geometrical approximations is described in Appendix D. Ionization timescales and electron density estimates are then used to calculate the age of the forward shock as $t = \tau/n_e$. The mean shock velocity is $\langle v_s \rangle = 855 \pm 100$ km s^{-1}, the electron density is $\langle n_e \rangle = (6 \pm 2)f^{-1/2}$ cm^{-3}, and the shock age is $\langle t \rangle = (1200 \pm 270)f^{-1/2}$ yr, where f represents the volume filling factor.

5.3. Deduction of Progenitor Mass

We estimate the mass of the progenitor with three different methods given in the literature using the spectral results from the interior regions.

5.3.1. Estimates from Nucleosynthesis Models

We can compare the yields obtained from the spectral fit of region e1 to models of low-metallicity CCSNe nucleosynthesis (Kobayashi et al. 2006; Nomoto et al. 2006)[7] in order to deduce the mass of the progenitor, as was investigated by Blair et al. (2000, see their Table 10). As we point out in Section 3, this is the only region that shows enhanced abundances of five of six elements that we fit across the remnant. Since direct model yields for LMC metallicity ($Z_{\rm LMC} = 0.008$) are not available in Nomoto et al. (2006) or Kobayashi et al. (2006), we take a geometric mean of model yields at SMC ($Z_{\rm SMC} = 0.004$) and Milky Way ($Z_{\rm MW} = 0.02$) metallicities to imitate the LMC environment. Kobayashi et al. (2011) updated the yields given by Kobayashi et al. (2006) for $Z = 0.004$, $18\,M_\odot$ and $Z = 0.02$, $25\,M_\odot$ models because the earlier models produced large amounts of ^{13}C and N due to erroneous mixing of H into the He-burning layer, also affecting the yields of other elements. Accordingly, we use the updated yields for these two models in our calculations.

We use the Mahalanobis distance and L_1 norm methods to find the measure of closeness between our observed yields and the yields predicted by the models. The Mahalanobis distance

---

[7] The same models and corresponding yields are reported in Kobayashi et al. (2006) and Nomoto et al. (2006).
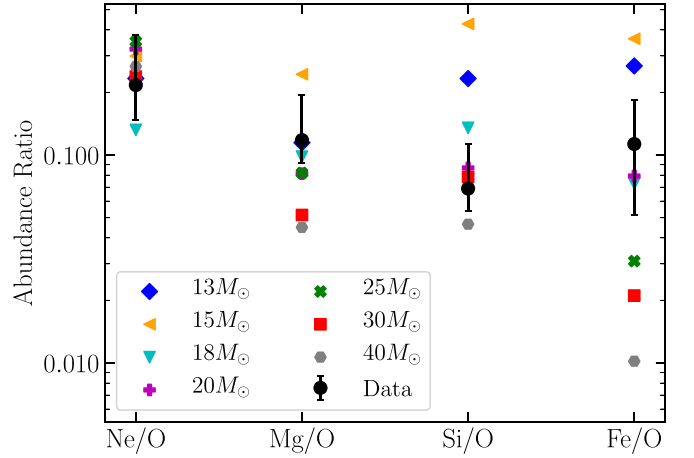
Figure 9. Abundances of different elements (relative to O) from the ejecta component of the best-fit model to the spectrum of region e1. Black markers denote the best-fit values, and colored markers denote the nucleosynthesis yields for different progenitor masses from Nomoto et al. (2006) and Kobayashi et al. (2006, 2011). The fit is presented in Table 5, and the spectrum is shown in Figure 7.

($M_{\rm D}$)

$$M_{\rm D} = \sqrt{\Sigma_{i=1}^n \frac{(x_i - y_i)^2}{s_i^2}} \qquad (2)$$

is essentially an error (s_i)-weighted Euclidean distance between the data (the test set x_i representing the observed yields from our work) and the various nucleosynthesis models (y_i; Mahalanobis 1936). The model yields are given in solar masses. Thus, to compare them with the best-fit values from the spectral fit to region e1, we convert the latter to elemental yields by multiplying them with atomic mass, since the reference scale is defined for the number of atoms relative to H and not the atomic mass. The test set is best explained by that model set for which the Mahalanobis distance is a minimum. The L_1 norm method works on a similar principle of distance minimization; its logarithmic form is given by (for example, Dopita et al. 2018, 2019)

$$L_1 = \frac{\sum_{j=1}^m |\log_{10} \frac{x_i}{y_i}|}{m}, \qquad (3)$$

where $m =$ number of elements. Figure 9 shows the abundance ratios relative to O for the different models and the data.[8] Model abundance ratios with a large scatter across progenitor masses (Si/O and Fe/O) drive the mass estimate because they show larger differences than other ratios that have relatively less scatter (Ne/O and Mg/O). While the Mahalanobis distance and L_1 norm are guided by Si/O for lower progenitor masses, they are largely set by Fe/O for massive progenitors. We present the comparison of progenitor mass deduction using the two methods in Figure 10. Note that both $M_{\rm D}$ and L_1 norm pass through the same global minimum as one moves from lower to higher mass progenitor models. Thus, we find a

---

[8] We note that the results do not change if we take abundance ratios with respect to Si instead of O, as is often done in such comparisons (for example, Kumar et al. 2014; Frank et al. 2015; Braun et al. 2019).
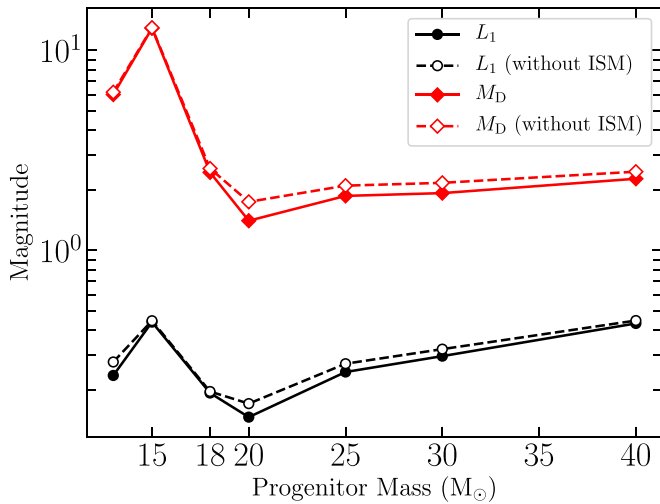
Figure 10. Magnitudes of L_1 norm and Mahalanobis distance (M_D) plotted against progenitor mass models in order to deduce the progenitor mass of N132D by comparing its "ejecta" yields with that given by the low-metallicity CCNSe nucleosynthesis models of Nomoto et al. (2006) and Kobayashi et al. (2006, 2011). The source model we use to find the best-fit parameters is the `vpshock+vnei` model; see Table 5. Dashed curves use the residual of best-fit abundances after we subtract the local average ISM contribution, to check for swept-up ISM contamination.

progenitor mass of $M_p = 20\,M_\odot$ to be the closest to our observed yields. The model yields we use are calculated for an explosion energy of 10^{51} erg. If the explosion energy for N132D was higher (Bamba et al. 2018), this will affect the comparison we make below because core-collapse models are very sensitive to the production of ^{56}Ni, which correlates with the explosion energy (Pejcha & Thompson 2015, see their Figure 20; Sukhbold et al. 2016, see their Figure 17). If the explosion energy was $>10^{51}$ erg, it will produce more Fe (Kobayashi et al. 2006; Nomoto et al. 2013). Further, these models are also sensitive to the rotation rate of the progenitor (Maeder & Meynet 2000; Tominaga et al. 2007; Nomoto et al. 2013).

Note that our deduction assumes that the region contains pure ejecta, which is an ideal case. Nonetheless, the ratios are not particularly sensitive to contamination from swept-up ISM. We verify this by subtracting the local average ISM values for each abundance and finding that both methods still have global minima at $20\,M_\odot$ (see the dashed lines in Figure 10). Although we utilize all possible elemental ratios to derive this estimate, we only use the X-ray-heated ejecta from a single region (which represents a tiny fraction of the remnant in projection) to estimate the progenitor mass in this manner. Thus, the yields in this region may not be representative of the entire remnant. However, in order to compare these yields against the CCSNe model yields, we require sufficiently high abundances of more than three elements to remove the degeneracy between models of diverse progenitor masses. Given the depth of the existing data, we find e1 to be the singular region that provides the most stringent constraints on these abundances. It is not surprising that we only find one eligible region for this analysis since such regions are difficult to extract because the remnant is dominated by swept-up ISM at the age of N132D. Given these caveats, it becomes clear why this technique is not sufficient to place robust constraints on the progenitor mass, and other avenues should be explored for the same.

Table 10
Estimates of the Progenitor Mass Based on Equation (4) from Katsuda et al. (2018b) That Depend on the Fe/Si Ratio Measured in the Ejecta Component in Spectral Models for the Interior Regions

Region ID	Ionizing Model	Recombining Model
e1	12.15^{+7}_{-4}	⋯
f1	9.65^{+7}_{-3}	10.67^{+3}_{-3}
f2	20.01^{+6}_{-2}	19.02^{+8}_{-5}
f3	12.65^{+5}_{-2}	12.66^{+5}_{-2}
f4	11.59^{+9}_{-4}	12.48^{+7}_{-3}
f5	16.70^{+4}_{-4}	17.93^{+3}_{-3}
f6	14.31^{+3}_{-2}	15.35^{+2}_{-2}

Note. Region e1 is only fit with a two-component (`vnei+vpshock`) model. Details of the estimation are presented in Section 5.3.2.

5.3.2. Estimates from Enriched Fe/Si

Katsuda et al. (2018b) point out that the estimates from elemental abundance ratios other than Fe/O or Fe/Si are not good tracers of progenitor mass because they are not sensitive to the CO core mass of the progenitor. Keeping this in mind, we also estimate the mass of the progenitor only from the Fe/Si ratio. As noted by Katsuda et al. (2018b), this technique cannot account for the unshocked ejecta in the SNR that can alter the measured Fe/Si ratio (see, however, Hwang & Laming 2012 and DeLaney et al. 2014, where it is proposed for SNR Cas A that up to 90% of its ejecta has already been shocked). A major advantage of only using the Fe/Si in our case is that apart from region e1, we can also use the Fe K regions since they show enhanced abundances of Fe/Si in the hottest model component that we assume comes largely from ejecta. Including these regions lets us cumulatively sample a large fraction of the remnant.

We use the best-fit relation provided by Katsuda et al. (2018b) that the authors find by fitting revised progenitor mass estimates for several SNRs in the Milky Way and the Magellanic Clouds against Fe/Si measured from observations:

$$\frac{\text{Fe/Si}}{\text{Fe/Si}_\odot} = 1.13 \times \exp\left(\frac{4.8 - M_p}{10.6}\right). \qquad (4)$$

Table 10 lists the progenitor mass estimates we derive from the spectral fits to regions e1 and f1–f6. We utilize the best-fit abundances of the highest electron temperature component in the ionizing and recombining models for these regions (see Section 4.2.2 and Table 7). The estimated best-fit masses from different regions lie between 10 and $20\,M_\odot$, with mean mass $\sim 15\,M_\odot$. The variation in the deduced progenitor mass from region to region provides some insight into the importance of sampling as much of the ejecta as possible, and the relatively large uncertainties on the deduced masses reflect the limitation imposed by the statistical precision of the current data.

5.3.3. Estimates from Explosion in a Cavity Models

Finally, we also estimate the progenitor mass using the relation between the radius of the cavity (R_b) and the progenitor mass (M_p) proposed by Chen et al. (2013) for SNRs evolving in

cavities in or near giant molecular clouds:

$$p_5^{1/3} R_b = \left[\alpha \left(\frac{M_p}{M_\odot} \right) - \beta \right] \text{pc},\tag{5}$$

where p_5 is the interclump pressure in units of $10^5 \, \text{cm}^{-3}$ K (assumed to be unity; see Blitz 1993; Chevalier 1999; Krumholz et al. 2009), and $\alpha = 1.22 \pm 0.05$ and $\beta = 9.16 \pm 1.77$ are derived from a linear regression. This assumes that the cavity was formed prior to the explosion by stellar winds of main-sequence OB stars (Hughes 1987) and does not take into account the effects of a Wolf–Rayet phase, if any, on the wind-blown bubble (Chevalier 2005). Although such CCSNe undergo significant mass loss prior to the explosion (Pastorello et al. 2008; Dwarkadas & Gruszko 2012; Milisavljevic et al. 2013; Kamble et al. 2016), its effect on the late-time dynamics when the blast wave interacts with the circumstellar shell has been shown to be of little importance (Patnaude et al. 2015, 2017). Thus, the predictions by an explosion in a cavity model like this for SNRs older than a few centuries may not be affected by the pre-supernova mass loss (Katsuda et al. 2018b). Since the shock has been interacting with the cloud in the south for the last few 100 yr (Chen et al. 2003), we assume that the radius of the cavity roughly equals the radius of X-ray emission. Adopting $R_p = 12.5$ pc, we derive $M_p = 17.\,8 \pm 3.8 \, M_\odot$, in agreement with the progenitor mass we determine above.

Note that the interclump pressure in N132D will be more than the thermal pressure since additional pressure support can arise from turbulence and cosmic rays in dynamically active regions like supernova remnants (Mac Low et al. 2005; Jenkins & Tripp 2011; Welty et al. 2016; Herrera-Camus et al. 2017). The average thermal pressure in the ISM of the LMC is estimated to be $p_{5,\text{th}} = 0.1$ (Welty et al. 2016). If we use this value as a lower limit on the interclump pressure, the minimum progenitor mass we obtain for the same cavity size is $\sim 12 \, M_\odot$, consistent with the results we summarize in Section 5.3.4.

5.3.4. Summary of Progenitor Mass Estimates

Estimation from different pathways (observational as well as theoretical) as we present above enables us to put a constraint on the progenitor mass. It is encouraging to find that the estimates of all three methods are within 2σ of each other. However, the results from nucleosynthesis yields and explosion in a cavity models favor a slightly more massive progenitor for N132D than the average estimated through the Fe/Si ratio. Nevertheless, our results suggest an intermediate-mass ($M_p < 25 \, M_\odot$) progenitor for N132D, lower than the estimates of Blair et al. (2000) based on UV/optical data (30–35 $M_\odot$) and by France et al. (2009) based on Cosmic Origins Spectrograph ($50^{+25}_{-15} \, M_\odot$) observations of N132D.

Taking into account the uncertainties and systematic scatter in all three methods listed above, we give our estimate of the progenitor mass of N132D as $M_p = 15 \pm 5 \, M_\odot$, in line with the revised mass estimates of Katsuda et al. (2018b). This range of possible progenitor masses also overlaps with the suggested range of massive stars that can undergo a Wolf–Rayet phase in the LMC (Chevalier 1999), as has been expected for N132D (Sutherland & Dopita 1995). Comparing with earlier predictions, we find that our progenitor mass estimate lies at the lower limit of Hwang et al. (1993), where the authors used Einstein

Observatory data of N132D and nucleosynthesis models of Thielemann et al. (1992) to propose a progenitor mass of 20–25 $M_\odot$, whereas it is consistent with the estimate of slightly less than 20 $M_\odot$ given by Blair et al. (1994).

If the mass of the progenitor was indeed within 10–20 $M_\odot$, this will have important implications for the explosion in a cavity scenario as well as the lifetime of the Wolf–Rayet phase, if any (van Marle & Keppens 2012). A possible avenue to explore through simulations is to estimate the time and size of the creation of a cavity by pre-supernova winds for the estimated progenitor mass (Tenorio-Tagle et al. 1991; Garcia-Segura et al. 1996; Dwarkadas 2007; Patnaude et al. 2017), but that is beyond the scope of this work.

5.4. High-temperature Plasma and Fe K Emission

Emission in the 6.5–6.9 keV band can be mostly attributed to the presence of Fe He-like (Fe XXV) line emission.[9] Suzaku observations of N132D provide the centroid line energy of Fe K emission as 6656 ± 9 eV (Yamaguchi et al. 2014), whereas XMM-Newton observations estimate it to be 6685^{+15}_{-14} eV (Maggi et al. 2016), proposed to be typical of middle-aged CCSNe (age >2500 yr) evolving in a dense CSM with high ambient densities (Yamaguchi et al. 2014; Patnaude et al. 2015). The Fe XXV He-like triplet spans about 64 eV between the recombination and forbidden lines. Thus, use of the ionizing or recombining model affects the relative strengths of these lines in this complex, but with the limited statistics and spectral resolution of the ACIS data we are not sensitive to a shift in the centroid.

From both the ionizing (vnei + vnei + vpshock) and recombining (vrnei + vnei + vpshock) models we use to fit the six regions (see Table 7) containing Fe K emission, we establish that a hotter ($\gtrsim 1.5$ keV) plasma is needed to explain the Fe K emission in this remnant, while not overproducing the flux from Fe L at lower energies. A similar observation was also made by Maggi et al. (2016). However, both models are able to explain this emission through hot NEI ionizing and recombining components, respectively. This degeneracy arises from the low number of counts in the hard X-ray band and the complex nature of the fit with many free parameters. Our results are consistent with the conclusions of the Suzaku + Hitomi investigation by Hitomi Collaboration et al. (2018) and the NuSTAR + Suzaku analysis by Bamba et al. (2018). However, we are able to sample smaller and more compact regions with Chandra than these studies to show that the Fe K emission is distributed throughout the southern half of the remnant (not concentrated in a single feature) and the plasma history is most likely different for different regions. Together with the enhanced abundances we find in other regions, this provides some evidence for an asymmetric explosion. However, the current Chandra data for N132D are not deep enough to reconstruct the ejecta distribution with sufficient precision to conclude that the explosion was indeed asymmetric. An

---

[9] Fe XXVI (Fe Li-like ion) also has certain line energies in the range 6.5–6.7 keV, but its emissivity is lower by at least an order of magnitude as compared to Fe XXV and becomes comparable only at temperatures $\lesssim 1.3$ keV, while the component accounting for Fe K emission in both the ionizing and recombining models is $\gtrsim 1.5$ keV. Moreover, for there to be significant flux from Fe XXVI, a high ionization rate for the Li-like stage (high temperature) is required, which cannot be possible near (optically thin coronal) equilibrium, not to mention that the process would anyway be unimportant in the recombining case. Thus, we can safely neglect the presence of significant flux from Fe Li-like ions in this energy range.

additional complication is the relatively large uncertainty in the explosion center for N132D, which is needed to constrain the ejecta distribution (Winkler & Petre 2007; Holland-Ashford et al. 2017; Katsuda et al. 2018a).

Although Fe K emission has been found in several SNRs in the LMC (Maggi et al. 2016, see their Table 2), the origin of a hotter plasma is not yet clear (see, for example, Park et al. 2005). Applying the Rankine–Hugoniot strong shock conditions to the individual species leads to mass-proportional heating, so $T_e \ll T_i$ (by the ratio m_e/m_i; see, for example, Shimada & Hoshino 2000). Coulomb equilibration (many small-angle scatterings) would give a characteristic equilibration timescale of $\sim$6000 yr, too slow to account for electrons hot enough to excite X-ray emission lines. This argues for collisionless equilibration–collective scattering of electrons with plasma magnetic field fluctuations. The available evidence is that this is effective for slow ($\lesssim$500 km s^{-1}) shocks, but falls as roughly $\propto v_s^{-2}$ and is much less effective for fast shocks. For example, for the estimated forward-shock velocity of 855 km s^{-1}, the ratio of electron to proton temperature is $\approx$0.2 (Ghavamian et al. 2007, 2013), indicating that the forward shock is unlikely to be the source of the Fe K emission. Presumably the reverse shock has a higher velocity into the ejecta with corresponding higher electron and ion temperatures than at the forward shock. For our fitted values of the temperature and ionization timescale, the RRC emission from Si and S would be weak. The Si and S RRCs would be stronger for lower plasma temperatures. We see no obvious RRC features for lower temperatures, so we can exclude that region of parameter space. Deeper observations may allow better constraints on anomalous line ratios for the He-like Fe and RRCs for lighter ions.

The high column densities of all of the Fe K regions except region f1 can be associated with the presence or absence of clumps of molecular clouds, respectively, as has been discussed for other SNRs interacting with molecular clouds (Banas et al. 1997; Lee et al. 2012; Slane et al. 2015; Matsumura et al. 2017; Sano et al. 2019). In fact, from Figure 2 of Dopita et al. (2018), we find that region f1 does not contain any prominent shocked ISM clouds as observed in the optical, which is expected for its low column density. Thus, the origin of a recombining plasma in this region, if any, can be correlated with thermal conduction only if we assume that the dense cloud(s) in this region have already been evaporated. If the recombining plasma is due to thermal conduction, one would expect it to be interacting with dense gas, which is likely the case for region f2. This analysis informs us of the spatially as well as spectrally diverse signatures of the plasma present in these regions that have evolved differently over time largely based on the surrounding environment. However, the origin of hot plasma that gives rise to the Fe K emission cannot be established from the available data.

6. Summary

In this work, we have presented spatially resolved X-ray spectroscopy of N132D, the brightest SNR in the LMC, based on archival Chandra observations. By fitting the spectra of the entire well-defined rim of the remnant with a plane-parallel shock model, we calculate the mean local abundances of O, Ne, Mg, Si, S, and Fe (Table 8) and find that Ne, Mg, Si, and Fe show no excess or depletion on the rim around their mean and the associated total (statistical+systematic) uncertainty,

whereas we find evidence of enhanced O and S on the northwestern and northeastern rims, respectively. A faint blob protruding outside the western rim shows enhanced abundance of O, but extended X-ray observations are needed to ascertain if this blob is in fact an O-rich ejecta clump moving ahead of the blast wave.

Using information from the rim regions, we derive a mean forward-shock velocity $\langle v_s \rangle = 855 \pm 100$ km s^{-1} and electron density $\langle n_e \rangle = (6 \pm 2) f^{-1/2}$ cm^{-3} where f is the volume filling factor. For $f \sim 1$, our findings agree with the conclusions of Chen et al. (2003), where the authors propose that the shock collided with the cavity wall (inside which the progenitor exploded) $\sim$700 yr ago, when it was slowed down from its precollision value of $\sim$1900 km s^{-1}. This is in line with the proposed explosion in a cavity scenario for this remnant, which partly comes from CO observations of molecular clouds in its surroundings (Banas et al. 1997; Sano et al. 2015).

We follow a mix of observational and theoretical approaches to estimate the mass of the progenitor of the remnant: (1) through comparison of best-fit ejecta abundances from region e1 with the nucleosynthesis model yields from Nomoto et al. (2006) and Kobayashi et al. (2006, 2011), (2) from Fe/Si ratios measured in the ejecta components of multiple regions in the interior (Katsuda et al. 2018b), and (3) predictions from theoretical models of a core-collapse explosion in a cavity within a molecular cloud complex (Chevalier 1999; Chen et al. 2013). Our estimated progenitor mass of $15 \pm 5 M_\odot$ is significantly lower than estimates based on optical data (Blair et al. 2000; France et al. 2009), but consistent with those of Katsuda et al. (2018b).

The presence of Fe K emission in N132D is well known (Behar et al. 2001; Xiao & Chen 2008; Yamaguchi et al. 2014; Maggi et al. 2016; Bamba et al. 2018; Hitomi Collaboration et al. 2018). With the spatial resolution of Chandra, we find that the Fe K complex emission is distributed largely across its southern half and is not located in a single feature. We fit the spectra of this emission in six regions using two different models that have three components each. These two models have two components in common, which account for the shell emission (plane-parallel shock) and cooler, soft X-ray emitting plasma (nonionization equilibrium). The third component, which accounts for the hotter, hard X-ray emitting plasma and Fe K emission, is a nonequilibrium ionizing plasma in one model and a recombining plasma in the other model. In both models, we find that a hot plasma ($\gtrsim$1.5 keV) is needed to explain the Fe K feature and that this plasma is distinct from the soft X-ray emitting plasma. While our fits cannot distinguish between the ionizing and recombining plasma models for these regions because they result in similar fit statistics, we confirm the existence of such a hot plasma, in agreement with the findings of Bamba et al. (2018). A deeper observation or an observation with higher spectral resolution will help break the degeneracy between the two models and possibly shed light on the origin of the hot plasma and its interactions with molecular clouds in the region.

Thus, our analysis leads us to conclude that SNR N132D probably resulted from the core collapse of an intermediate-mass progenitor, in a cavity in the CSM created by pre-supernova winds. The exact type of the explosion, the possibility of a Wolf–Rayet phase prior to it, and the nature of the hot Fe K emitting plasma are some of the pertinent questions that still remain unanswered. Deeper observations

with existing instruments and future observations with new instruments with enhanced capabilities will be required to address these questions.
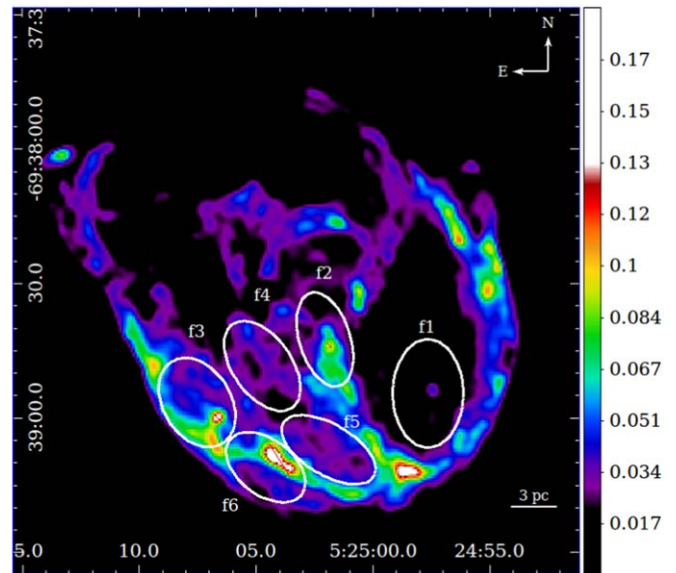
Appendix A
Pileup Map and Narrowband Images

Figure A1 shows the pileup fraction in the remnant. Note that CIAO estimates the pileup in an image without filtering over energy. Figure A2 shows the narrowband images around various bright line emissions of O, Ne, Mg, Si, S, and Fe in the remnant.

Figure A1. Pileup map of SNR N132D from 2006 Chandra archival observations. The color bar denotes the pileup fraction calculated in CIAO over all energies. The bright patches that are significantly affected by pileup in regions f2, f3, and f6 are excluded from the X-ray analysis.

20
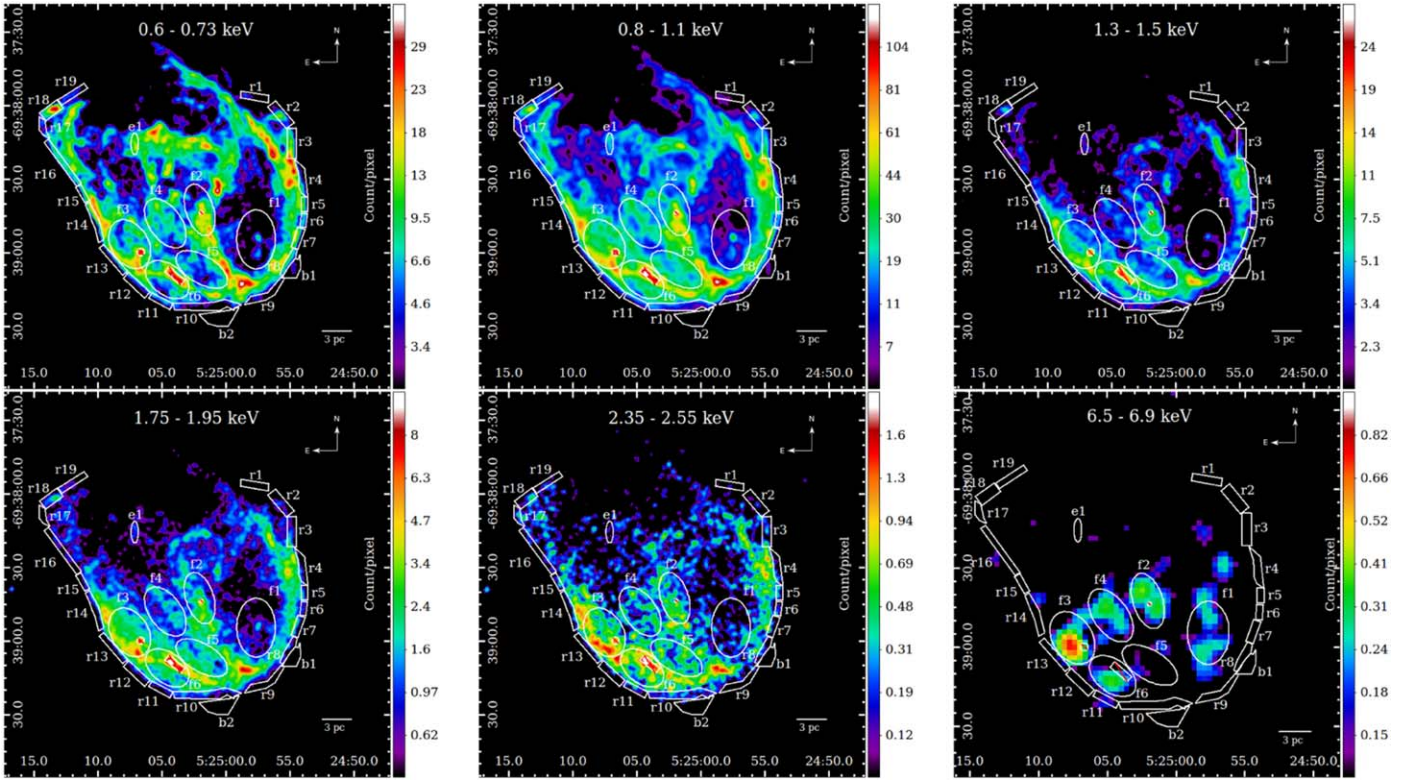
Figure A2. Narrowband images of SNR N132D from Chandra 2006 archival observations, with bands covering (top, left to right) the brightest line emissions of O, Ne, and Mg, and (bottom, left to right) Si, S, and Fe. All images have been smoothed with a Gaussian kernel of radius 3, except for Fe, where it has been binned by 4 and smoothed with a kernel of radius 3 owing to weak Fe K emission. Note that Fe also has numerous L-shell lines around 1 keV.

Appendix B
Error and Scatter on the Mean Using Multiple Imputations

We use the method of Multiple Imputations (Lee et al. 2011) to get an estimate of 68% confidence intervals (similar to 1σ in the Gaussian case) for the mean values calculated for the blast wave spectral parameters across the rim of the remnant (see Table 6). This method incorporates systematic uncertainties caused by scatter among the best-fit values in different regions along with standard statistical uncertainties in the estimates of each parameter. Thus, it is a better descriptor of the scatter present in the samples. Further, it also lets us quantify the systematic variations of a parameter around the rim. We estimate the combined statistical and systematic uncertainty by computing the weighted average (see Section 3.1.2 of Lee et al. 2011) of the so-called "between" variance (B, the variance of the best-fit values and a measure of the systematic scatter present in the data) and the "within" variance (W, the average of the individual variances in each measurement, and a measure of the statistical quality of the data) as follows:

$$V = W + \left(1 + \frac{1}{M}\right)B, \qquad (B1)$$

where M is the number of regions, and $\sqrt{V}$ represents the width of a t_ν-distribution with ν degrees of freedom:

$$\nu = (M - 1)\left(1 + \frac{M \cdot W}{(M + 1)B}\right)^2. \qquad (B2)$$

The t_ν-distribution has inherently heavier tails than the Gaussian distribution, but it closely approximates the width

of the latter for large ν ($\gtrsim 7$). We compute a correction factor C_ν to map the 84th-percentile quantile of the t_ν-distribution to $\sqrt{V}$ and define a 1σ-equivalent error bar

$$\sigma_\mu = C_\nu \times \sqrt{V}. \qquad (B3)$$

We find $\nu \in \{20, 79\}$ for the various parameters considered. The correction factor $C_\nu \to 1$ as $\nu \to \infty$ and is $\approx 2\%$ for $\nu = 20$. These 1σ-equivalent error bars are reported in Table 6.

The separation of the statistical (W) and systematic (B) variances also allows us to explore when systematic variations are large compared to the accuracy with which the parameters are measured. Large values of the scatter, $\frac{\sqrt{B}}{\sqrt{W}}$, show where systematic variations overwhelm the statistical error (see Table 6). When scatter >1, there is more systematic than statistical uncertainty in the parameter value, implying the presence of localized variations. We consider all abundance samples where this threshold is exceeded as showing localized enhancements.

Appendix C
Spectral Fits

Figures C1–C10 display the spectral fits and residuals for rim regions with the vpshock model (regions r2, r4–r9, r11–r19, b1, and b2) and the vnei+vpshock model (regions r3 and r10). Figures C11–C15 present the spectral fits for the Fe K regions. Note that the spectral counts in all plots have been rebinned for display purposes.
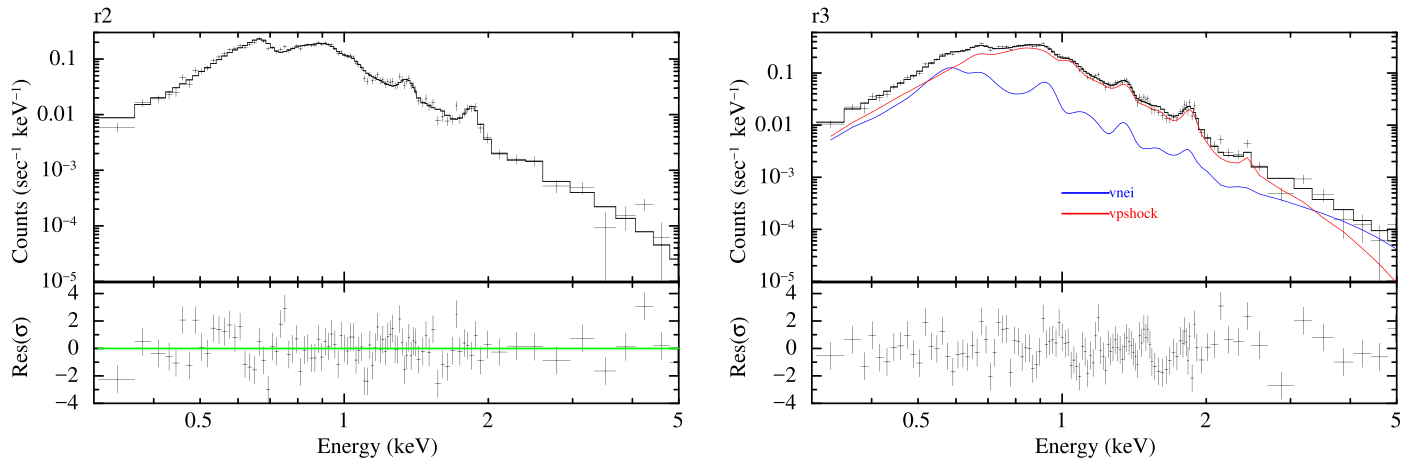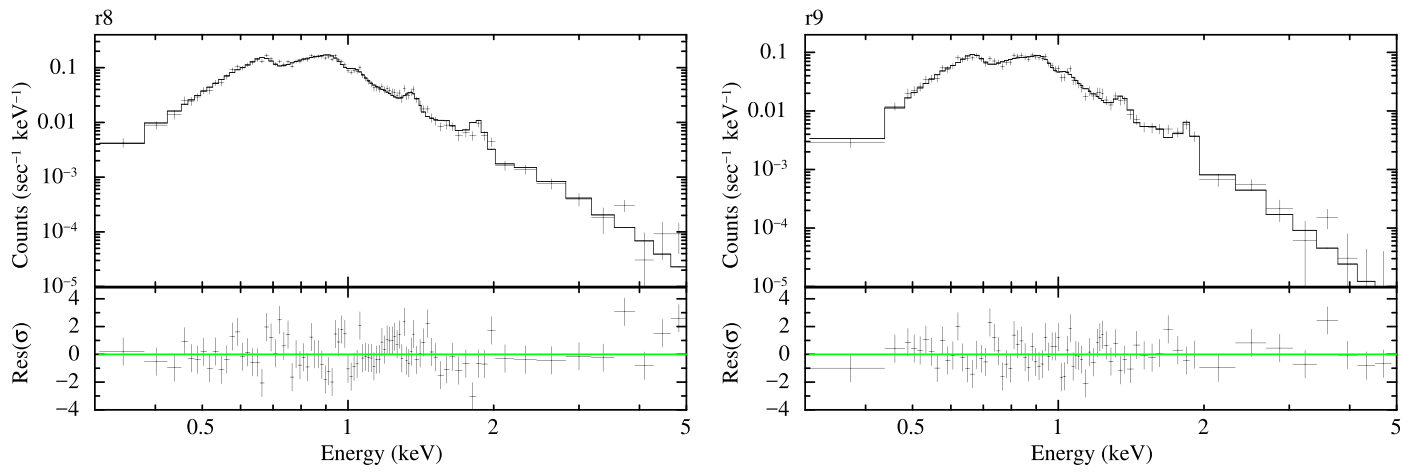
Figure C1. Fits for regions r2 and r3 with the single `vpshock` and `vnei+vpshock` models, respectively.
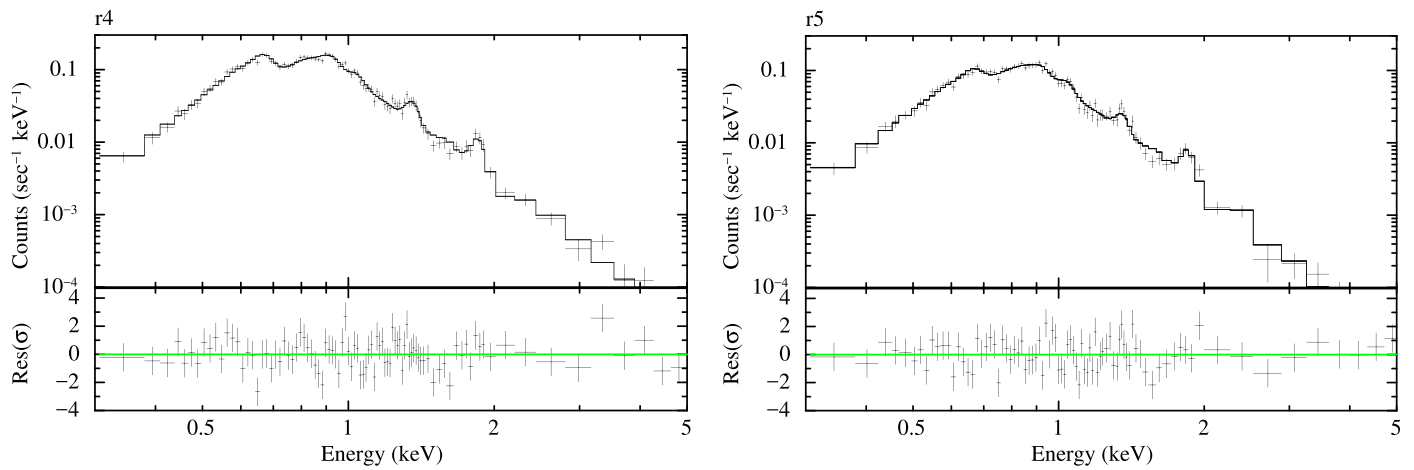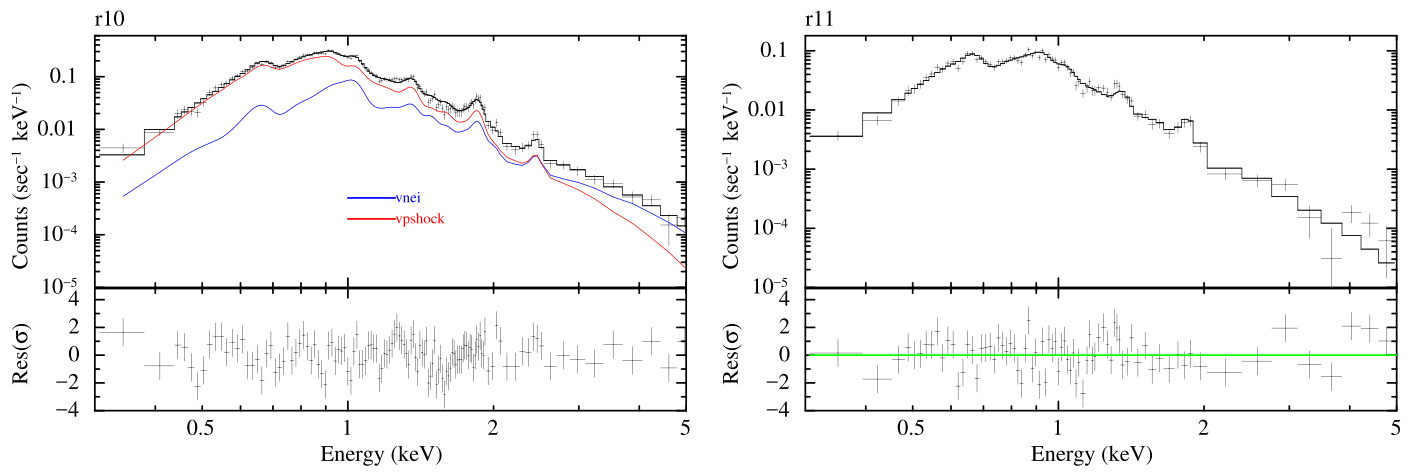

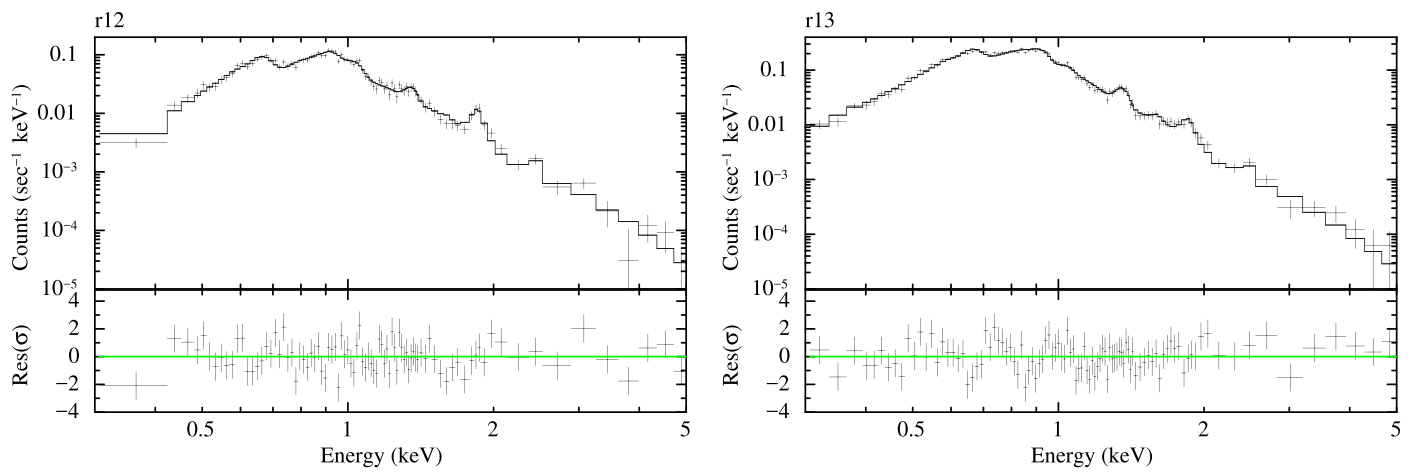**Figure C2.** Fits for regions r4 and r5 with the single `vpshock`.
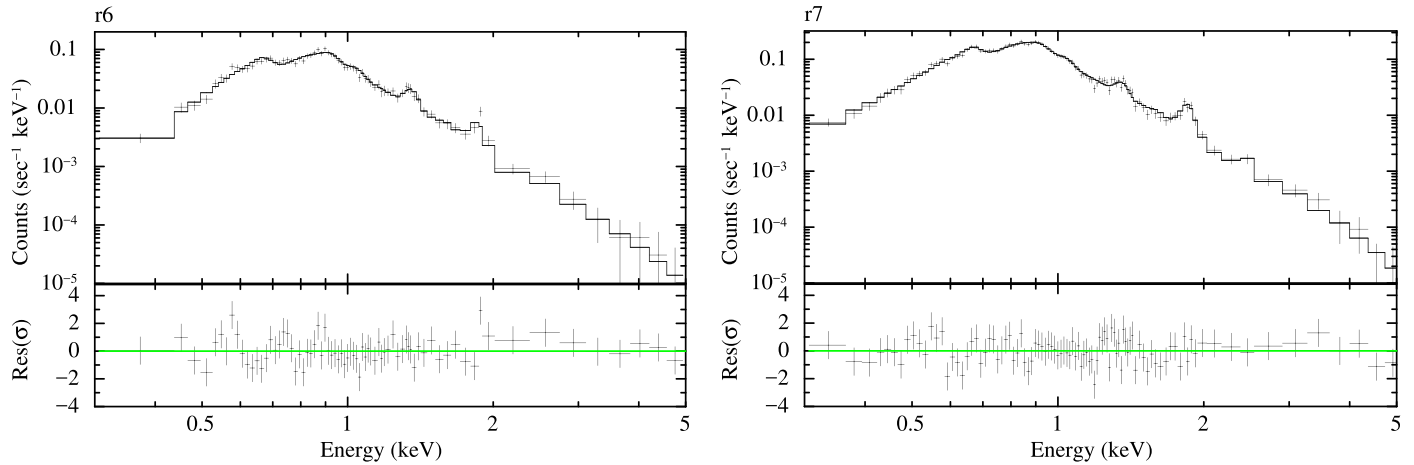
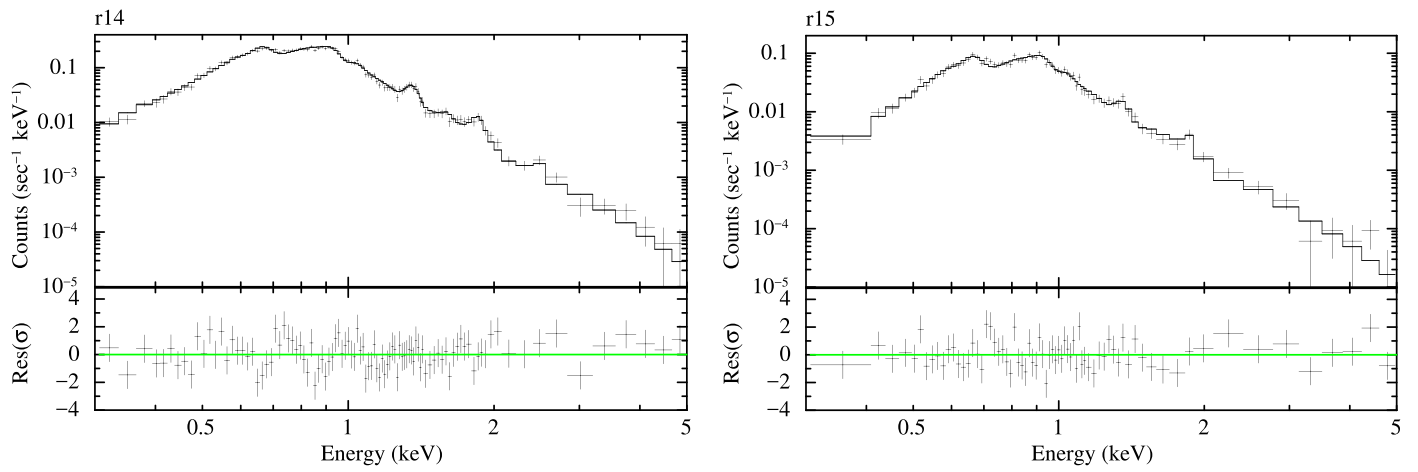**Figure C3.** Fits for regions r6 and r7 with the single `vpshock`.

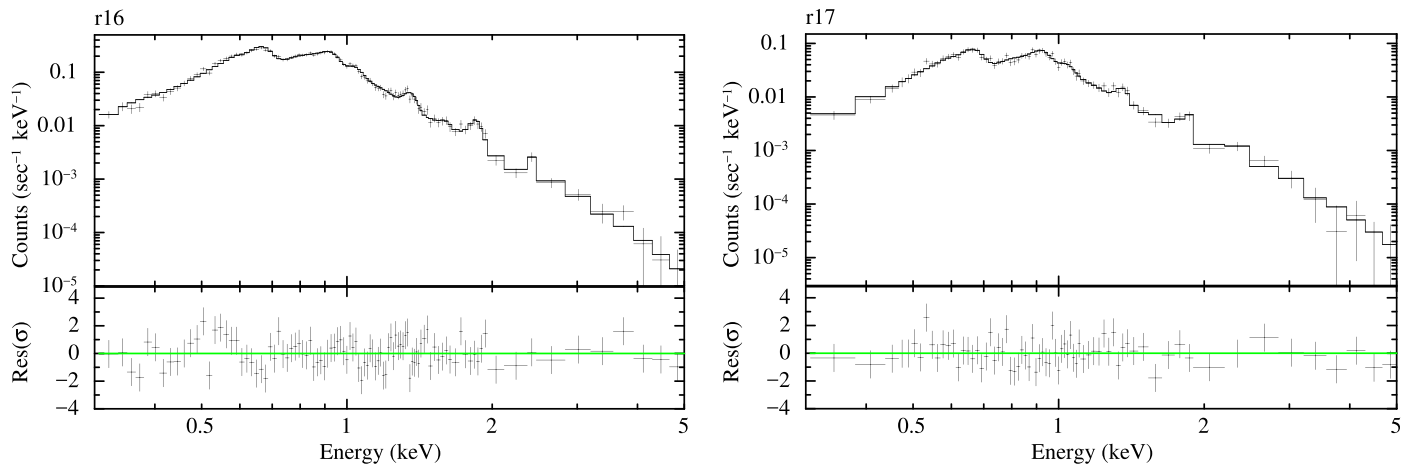**Figure C4.** Fits for regions r8 and r9 with the single `vpshock`.

Figure C5. Fits for regions r10 and r11 with the `vnei+vpshock` and the single `vpshock` models, respectively.
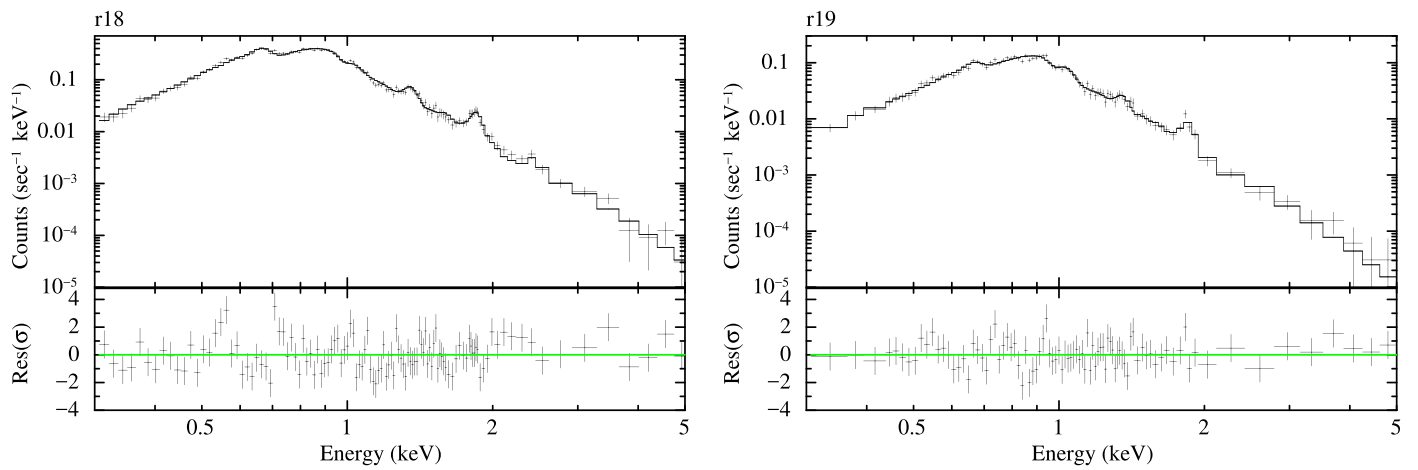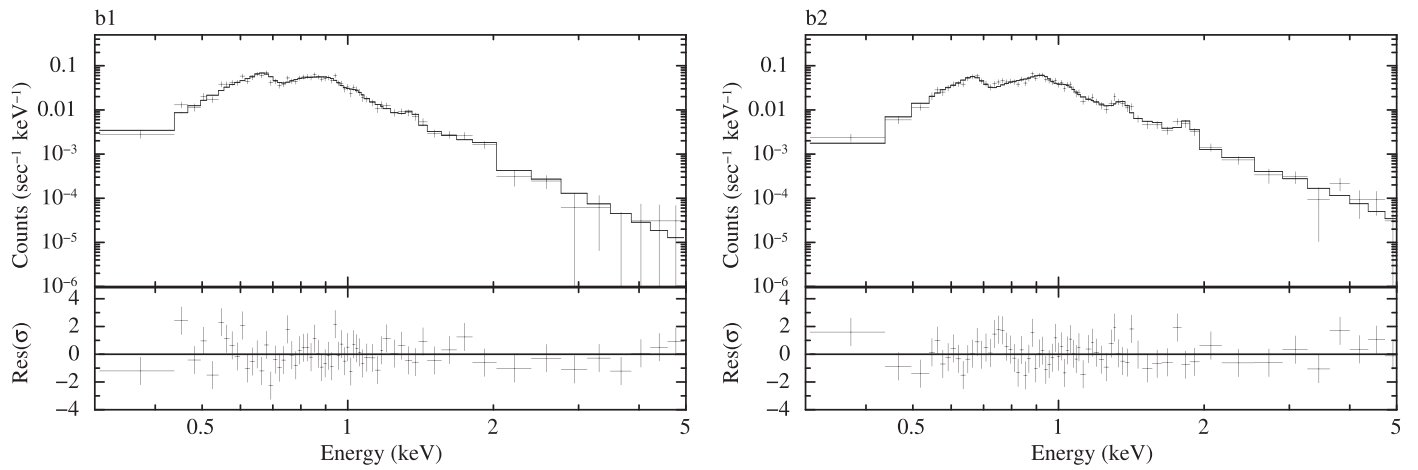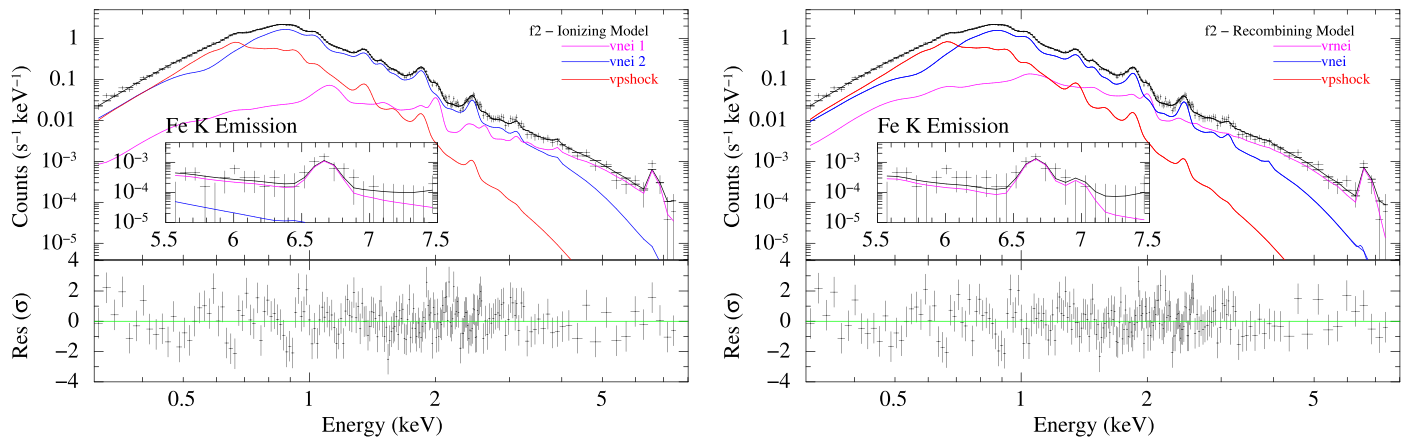

Figure C6. Fits for regions r12 and r13 with the single `vpshock`.

Figure C7. Fits for regions r14 and r15 with the single `vpshock`.

Figure C8. Fits for regions r16 and r17 with the single `vpshock`.

Figure C9. Fits for regions r18 and r19 with the single `vpshock`.

Figure C10. Fits for blobs b1 and b2 protruding ahead of the western rim with the single `vpshock` model.

Figure C11. Same as Figure 8, but for the region f2.
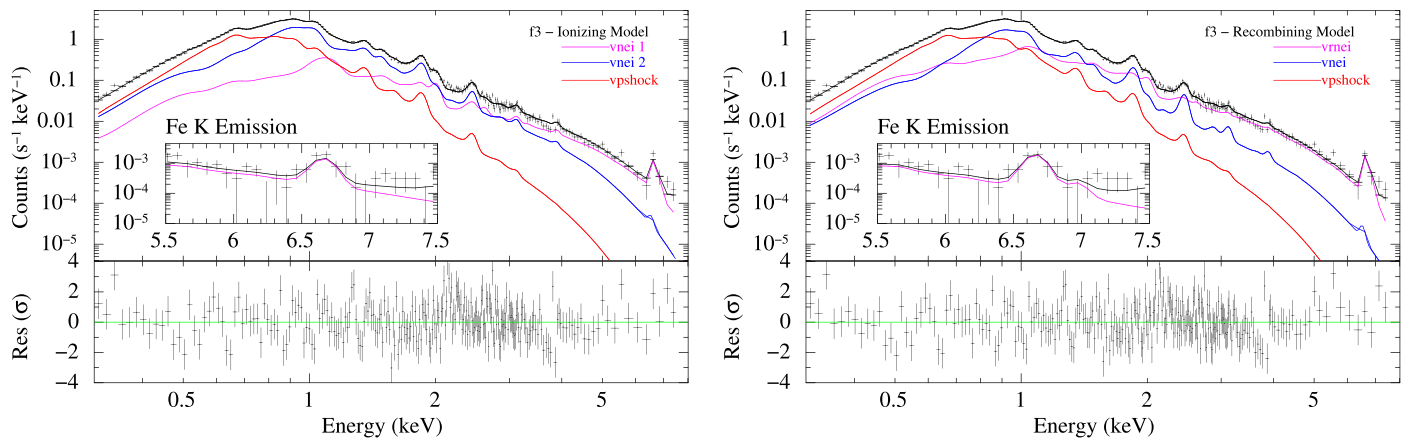
Figure C12. Same as Figure 8, but for the region f3.
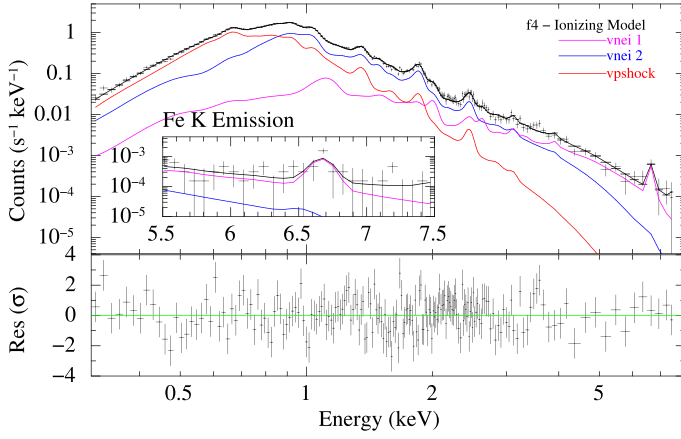
Figure C13. Same as Figure 8, but for the region f4.
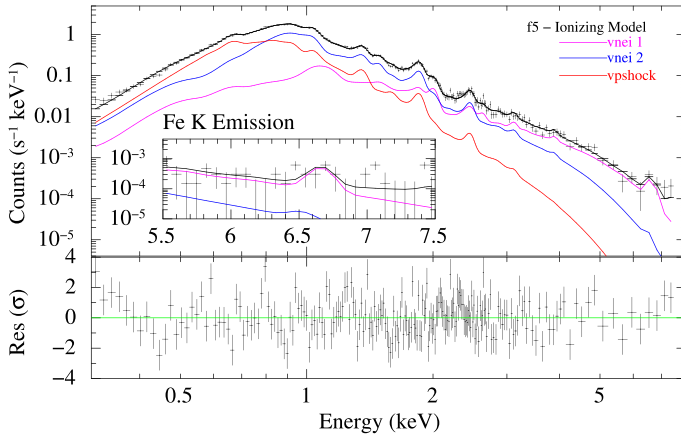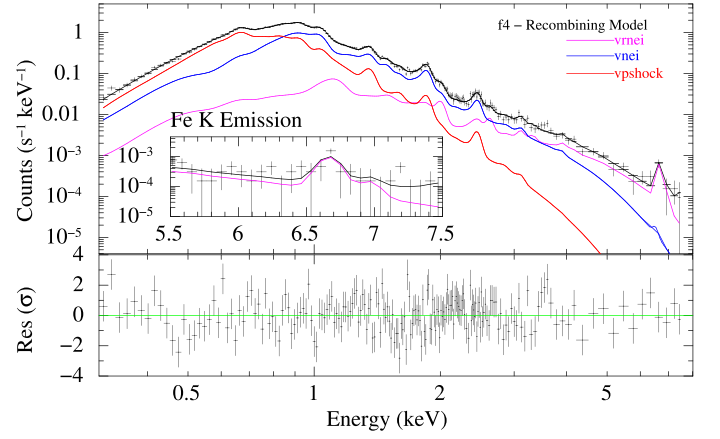
Figure C14. Same as Figure 8, but for the region f5.
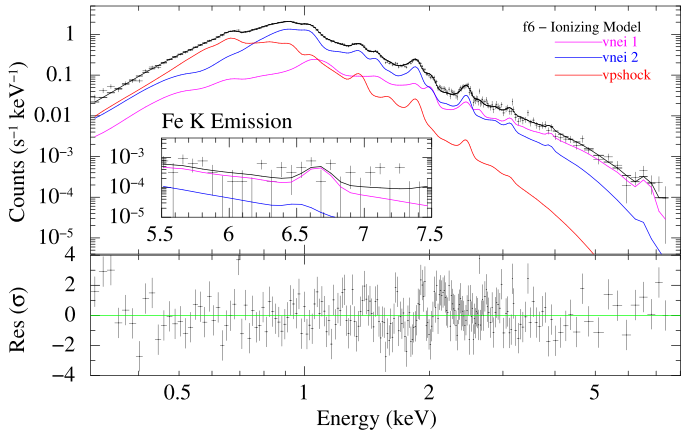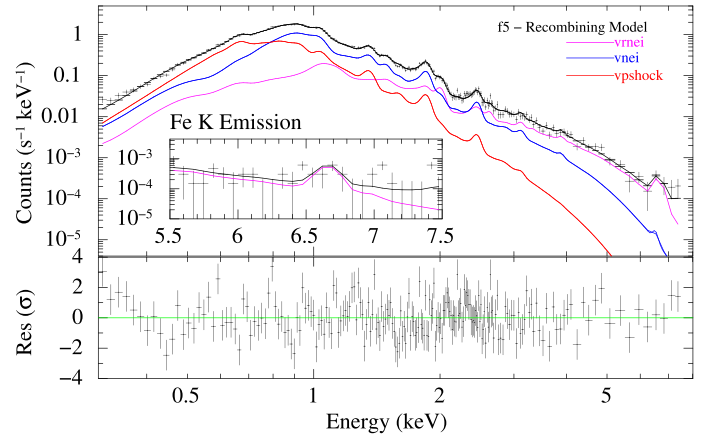
Figure C15. Same as Figure 8, but for the region f6.
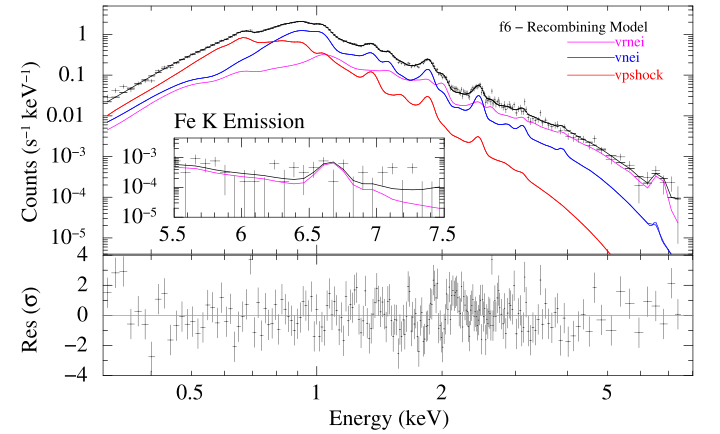
Appendix D
Electron Density Calculation

For thermal plasma models, the `Xspec` normalization, `norm`, is proportional to the emission measure as $\text{norm} \propto \int dV n_e n_H \sim \langle n_e^2 \rangle f \Delta V$. Here, we assume $n_e \sim 1.2\, n_H$ (see, for example, Schenck et al. 2014; however, this will be a lower limit if a considerable quantity of metals is present), $\langle n_e^2 \rangle$ is an average n_e^2, f is the volume filling factor for the emitting

region, and ΔV is the volume corresponding to the extraction region, that is, the projected area, $A = wh$, where w and h are the width and height of the extraction region, times an average line-of-sight depth, $\langle l \rangle$. To estimate the volume, some assumption is needed about the local three-dimensional structure. If the extraction region is assumed to be locally a projection through a figure of revolution with its axis in the plane of the sky (see Figure D1), the cross-sectional area can
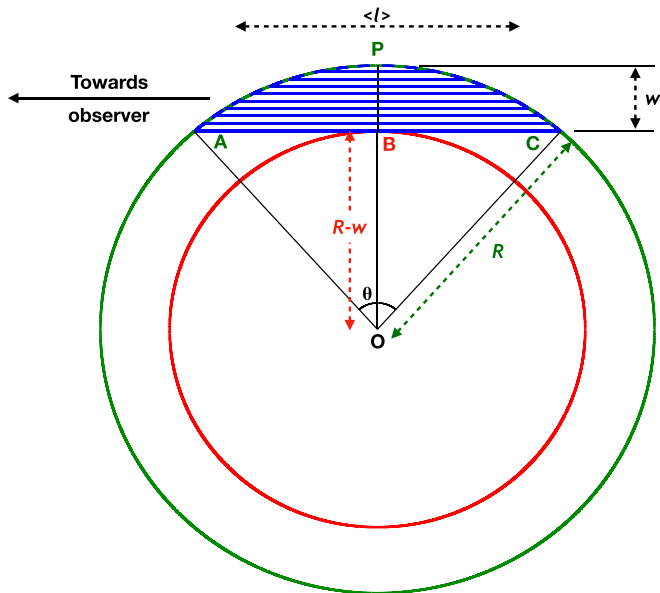
Figure D1. Sketch of the geometry assumed for the calculation of the depth $\langle l \rangle$ of the regions used for spectral fitting along the rim. The blue shaded area, enclosed between the arc APC and the horizontal line AC, depicts the region along the line of sight, pictured in cross section as part of a circular cylindrical shell defined by the green outer circle and the red inner circle. The opening angle AOC $\equiv \theta$ is determined by the width w and the distance of the region from the center of the remnant R. The shaded area is the difference between the pie-shaped region AOCPA and the triangle AOCBA.

be expressed as

$$A_\mathrm{c} = R^2 \cos^{-1}\left(\frac{R-w}{w}\right) - (R-w)\sqrt{2Rw - w^2}, \quad \text{(D1)}$$

where R is the radius of the circular segment of width w. The average line-of-sight depth $\langle l \rangle$ can then be estimated by dividing this area by the width w of the extraction region, and the volume is then estimated by $\langle l \rangle$ times the area of the extraction region. Thus, $n_e \sim \langle 1.2\, n_e^2 \rangle^{1/2} \sim 1106\,(\texttt{norm}/f\Delta V)^{1/2}\,\mathrm{cm}^{-3}$, where $\texttt{norm}$ is in units of cm^{-5} and ΔV is in units of pc^3.

ORCID iDs

Piyush Sharda ⬤ https://orcid.org/0000-0003-3347-7094
Terrance J. Gaetz ⬤ https://orcid.org/000-0002-5115-1533
Vinay L. Kashyap ⬤ https://orcid.org/0000-0002-3869-7996
Paul P. Plucinsky ⬤ https://orcid.org/0000-0003-1415-5823

References

Acero, F., Ackermann, M., Ajello, M., et al. 2016, ApJS, 224, 8
Ackermann, M., Albert, A., Atwood, W. B., et al. 2016, A&A, 586, A71
Arnaud, K. A. 1996, in ASP Conf. Ser. 101, Astronomical Data Analysis Software and Systems V, ed. G. H. Jacoby & J. Barnes (San Francisco, CA: ASP), 17
Auchettl, K., Ng, C.-Y., Wong, B. T. T., Lopez, L., & Slane, P. 2017, ApJ, 847, 121
Ballet, J. 1999, A&AS, 135, 371
Bamba, A., Ohira, Y., Yamazaki, R., et al. 2018, ApJ, 854, 71
Banas, K. R., Hughes, J. P., Bronfman, L., & Nyman, L.-Å. 1997, ApJ, 480, 607
Bartalucci, I., Mazzotta, P., Bourdin, H., & Vikhlinin, A. 2014, A&A, 566, A25
Bautz, M. W., Pivovaroff, M., Baganoff, F., et al. 1998, Proc. SPIE, 3444, 210
Bearden, J. A. 1967, RvMP, 39, 78
Behar, E., Rasmussen, A. P., Griffiths, R. G., et al. 2001, A&A, 365, L242

Berezhko, E. G., & Ellison, D. C. 1999, ApJ, 526, 385
Blackburn, J. K. 1995, in ASP Conf. Ser. 77, FTOOLS: A FITS Data Processing and Analysis Software Package, ed. R. A. Shaw, H. E. Payne, & J. J. E. Hayes (San Francisco, CA: ASP), 367
Blair, W. P., Morse, J. A., Raymond, J. C., et al. 2000, ApJ, 537, 667
Blair, W. P., Raymond, J. C., & Long, K. S. 1994, ApJ, 423, 334
Blitz, L. 1993, in Protostars and Planets III, ed. E. H. Levy & J. I. Lunine (Tucson, AZ: Univ. Arizona Press), 125
Borkowski, K. J., Hendrick, S. P., & Reynolds, S. P. 2007, ApJL, 671, L45
Borkowski, K. J., Lyerly, W. J., & Reynolds, S. P. 2001, ApJ, 548, 820
Braun, C., Safi-Harb, S., & Fryer, C. L. 2019, MNRAS, 489, 4444
Cash, W. 1979, ApJ, 228, 939
Chen, L. W., Fabian, A. C., & Gendreau, K. C. 1997, MNRAS, 285, 449
Chen, Y., Zhang, F., Williams, R. M., & Wang, Q. D. 2003, ApJ, 595, 227
Chen, Y., Zhou, P., & Chu, Y.-H. 2013, ApJL, 769, L16
Chevalier, R. A. 1999, ApJ, 511, 798
Chevalier, R. A. 2005, ApJ, 619, 839
Clementini, G., Gratton, R., Bragaglia, A., et al. 2003, AJ, 125, 1309
Danziger, I. J., & Dennefeld, M. 1976, ApJ, 207, 394
Davis, J. E. 2001, ApJ, 562, 575
DeLaney, T., Kassim, N. E., Rudnick, L., & Perley, R. A. 2014, ApJ, 785, 7
Desai, K. M., Chu, Y.-H., Gruendl, R. A., et al. 2010, AJ, 140, 584
Dickel, J. R., & Milne, D. K. 1995, AJ, 109, 200
Dickey, J. M., & Lockman, F. J. 1990, ARA&A, 28, 215
Dopita, M., Rhee, J., Farage, C., et al. 2010, Ap&SS, 327, 245
Dopita, M. A., Seitenzahl, I. R., Sutherland, R. S., et al. 2019, AJ, 157, 50
Dopita, M. A., Vogt, F. P. A., Sutherland, R. S., et al. 2018, ApJS, 237, 10
Dufour, R. J., Shields, G. A., & Talbot, R. J., Jr. 1982, ApJ, 252, 461
Dwarkadas, V. V. 2007, ApJ, 667, 226
Dwarkadas, V. V., & Gruszko, J. 2012, MNRAS, 419, 1515
Ellison, D. C., Patnaude, D. J., Slane, P., Blasi, P., & Gabici, S. 2007, ApJ, 661, 879
Favata, F., Vink, J., Parmar, A. N., Kaastra, J. S., & Mineo, T. 1997, A&A, 324, L45
Foster, A. R., Ji, L., Yamaguchi, H., Smith, R. K., & Brickhouse, N. S. 2013, in AIP Conf. Ser. 1545, Eighth International Conference on Atomic and Molecular Data and their Applications , ed. J. D. Gillaspy, W. L. Wiese, & Y. A. Podpaly (Melville, NY: AIP), 252
France, K., Beasley, M., Keeney, B. A., et al. 2009, ApJL, 707, L27
Frank, K. A., Burrows, D. N., & Park, S. 2015, ApJ, 810, 113
Fruscione, A., McDowell, J. C., Allen, G. E., et al. 2006, Proc. SPIE, 6270, 62701V
Fukui, Y., Kawamura, A., Minamidani, T., et al. 2008, ApJS, 178, 56
Gaetz, T. J. 1990, ApJ, 353, 245
Garcia-Segura, G., Langer, N., & Mac Low, M.-M. 1996, A&A, 316, 133
Garofali, K., Williams, B. F., Plucinsky, P. P., et al. 2017, MNRAS, 472, 308
Ghavamian, P., Hughes, J. P., & Williams, T. B. 2005, ApJ, 635, 365
Ghavamian, P., Laming, J. M., & Rakowski, C. E. 2007, ApJL, 654, L69
Ghavamian, P., Schwartz, S. J., Mitchell, J., Masters, A., & Laming, J. M. 2013, SSRv, 178, 633
Graessle, D. E., Evans, I. N., Glotfelty, K., et al. 2007, ChNew, 14, 33
Hamilton, A. J. S., Sarazin, C. L., & Chevalier, R. A. 1983, ApJS, 51, 115
Henize, K. G. 1956, ApJS, 2, 315
Herrera-Camus, R., Bolatto, A., Wolfire, M., et al. 2017, ApJ, 835, 201
H.E.S.S. Collaboration, Abramowski, A., Aharonian, F., et al. 2015, Sci, 347, 406
Higdon, J. C., & Lingenfelter, R. E. 1980, ApJ, 239, 867
Hitomi Collaboration, Aharonian, F., Akamatsu, H., et al. 2018, PASJ, 70, 16
Holland-Ashford, T., Lopez, L. A., Auchettl, K., Temim, T., & Ramirez-Ruiz, E. 2017, ApJ, 844, 84
Hughes, J. P. 1987, ApJ, 314, 103
Hughes, J. P., Hayashi, I., & Koyama, K. 1998, ApJ, 505, 732
Hunter, J. D. 2007, CSE, 9, 90
Hwang, U., Hughes, J. P., Canizares, C. R., & Markert, T. H. 1993, ApJ, 414, 219
Hwang, U., & Laming, J. M. 2012, ApJ, 746, 130
Itoh, H. 1977, PASJ, 29, 813
Itoh, H., & Masai, K. 1989, MNRAS, 236, 885
Jenkins, E. B., & Tripp, T. M. 2011, ApJ, 734, 65
Jones, F. C., & Ellison, D. C. 1991, SSRv, 58, 259
Joye, W. A., & Mandel, E. 2003, in ASP Conf. Ser. 295, Astronomical Data Analysis Software and Systems XII, ed. H. E. Payne, R. I. Jedrzejewski, & R. N. Hook (San Francisco, CA: ASP), 489
Kaastra, J. S. 2017, A&A, 605, A51
Kamble, A., Margutti, R., Soderberg, A. M., et al. 2016, ApJ, 818, 111
Kamitsukasa, F., Koyama, K., Uchida, H., et al. 2015, PASJ, 67, 16

Kashyap, V., & Drake, J. J. 2000, BASI, 28, 475
Katsuda, S., Morii, M., Janka, H.-T., et al. 2018a, ApJ, 856, 18
Katsuda, S., Takiwaki, T., Tominaga, N., Moriya, T. J., & Nakamura, K. 2018b, ApJ, 863, 127
Katsuragawa, M., Nakashima, S., Matsumura, H., et al. 2018, PASJ, 70, 110
Kavanagh, P. J., Sasaki, M., Breitschwerdt, D., et al. 2020, A&A, 637, 12
Kawasaki, M. T., Ozaki, M., Nagase, F., et al. 2002, ApJ, 572, 897
Kim, S., Staveley-Smith, L., Dopita, M. A., et al. 2003, ApJS, 148, 473
Kobayashi, C., Karakas, A. I., & Umeda, H. 2011, MNRAS, 414, 3231
Kobayashi, C., Umeda, H., Nomoto, K., Tominaga, N., & Ohkubo, T. 2006, ApJ, 653, 1145
Korn, A. J., Keller, S. C., Kaufer, A., et al. 2002, A&A, 385, 143
Krumholz, M. R., McKee, C. F., & Tumlinson, J. 2009, ApJ, 699, 850
Kumar, H. S., Safi-Harb, S., Slane, P. O., & Gotthelf, E. V. 2014, ApJ, 781, 41
Kuntz, K. D., & Snowden, S. L. 2001, ApJ, 554, 684
Kuntz, K. D., & Snowden, S. L. 2010, ApJS, 188, 46
Lakićević, M., van Loon, J. T., Meixner, M., et al. 2015, ApJ, 799, 50
Landau, L. D., & Lifshitz, E. M. 1975, The Classical Theory of Fields (Oxford: Pergamon Press)
Lasker, B. M. 1978, ApJ, 223, 109
Lasker, B. M. 1980, ApJ, 237, 765
Law, C. J., Milisavljevic, D., Patnaude, D. J., et al. 2020, ApJ, 894, 73
Leccardi, A., & Molendi, S. 2007, A&A, 472, 21
Lee, H., Kashyap, V. L., van Dyk, D. A., et al. 2011, ApJ, 731, 126
Lee, J.-J., Koo, B.-C., Snell, R. L., et al. 2012, ApJ, 749, 34
Long, K. S., & Helfand, D. J. 1979, ApJL, 234, L77
Lopez, L. A., Pearson, S., Ramirez-Ruiz, E., et al. 2013, ApJ, 777, 145
Mac Low, M.-M., Balsara, D. S., Kim, J., & de Avillez, M. A. 2005, ApJ, 626, 864
Maeder, A., & Meynet, G. 2000, ARA&A, 38, 143
Maggi, P., Filipović, M. D., Vukotić, B., et al. 2019, A&A, 631, A127
Maggi, P., Haberl, F., Kavanagh, P. J., et al. 2016, A&A, 585, A162
Mahalanobis, P. C. 1936, Proc. Natl. Inst. Sci. India, 2, 49
Masai, K. 1994, ApJ, 437, 770
Matsumura, H., Tanaka, T., Uchida, H., Okon, H., & Tsuru, T. G. 2017, ApJ, 851, 73
McCammon, D., Almy, R., Apodaca, E., et al. 2002, ApJ, 576, 188
McKee, C. F. 1974, ApJ, 188, 335
Mewe, R., & Gronenschild, E. H. B. M. 1981, A&AS, 45, 11
Milisavljevic, D., Law, C. J., Patnaude, D., et al. 2020, AAS Meeting, 52, 307.08
Milisavljevic, D., Margutti, R., Soderberg, A. M., et al. 2013, ApJ, 767, 71
Morse, J. A., Blair, W. P., Dopita, M. A., et al. 1996, AJ, 112, 2350
Morse, J. A., Winkler, P. F., & Kirshner, R. P. 1995, AJ, 109, 2104
Nomoto, K., Kobayashi, C., & Tominaga, N. 2013, ARA&A, 51, 457
Nomoto, K., Tominaga, N., Umeda, H., Kobayashi, C., & Maeda, K. 2006, NuPhA, 777, 424
Nousek, J. A., & Shue, D. R. 1989, ApJ, 342, 1207
Okon, H., Tanaka, T., Uchida, H., et al. 2020, ApJ, 890, 62
Okon, H., Uchida, H., Tanaka, T., Matsumura, H., & Tsuru, T. G. 2018, PASJ, 70, 35
Oliphant, T. E. 2006, A Guide to NumPy, Vol. 1 (USA: Trelgol Publishing)
Ozawa, M., Koyama, K., Yamaguchi, H., Masai, K., & Tamagawa, T. 2009, ApJL, 706, L71
Park, S., Muno, M. P., Baganoff, F. K., et al. 2005, ApJ, 631, 964
Pastorello, A., Mattila, S., Zampieri, L., et al. 2008, MNRAS, 389, 113
Patnaude, D. J., & Fesen, R. A. 2014, ApJ, 789, 138
Patnaude, D. J., Lee, S.-H., Slane, P. O., et al. 2015, ApJ, 803, 101
Patnaude, D. J., Lee, S.-H., Slane, P. O., et al. 2017, ApJ, 849, 109
Pejcha, O., & Thompson, T. A. 2015, ApJ, 801, 90
Pietrzyński, G., Graczyk, D., Gallenne, A., et al. 2019, Natur, 567, 200
Pietrzyński, G., Graczyk, D., Gieren, W., et al. 2013, Natur, 495, 76
Porquet, D., Dubau, J., & Grosso, N. 2010, SSRv, 157, 103

Rho, J., & Petre, R. 1998, ApJL, 503, L167
Russell, S. C., & Dopita, M. A. 1992, ApJ, 384, 508
Sano, H. 2019, ALMA2019: Science Results and Cross-Facility Synergies (Munich: ESO), 123
Sano, H., Fukui, Y., Yoshiike, S., et al. 2015, in ASP Conf. Ser. 499, Revolution in Astronomy with ALMA: The Third Year, ed. D. Iono et al. (San Francisco, CA: ASP), 257
Sano, H., Matsumura, H., Yamane, Y., et al. 2019, ApJ, 881, 85
Schenck, A., Park, S., Burrows, D. N., et al. 2014, ApJ, 791, 50
Schenck, A., Park, S., & Post, S. 2016, AJ, 151, 161
Seok, J. Y., Koo, B.-C., & Onaka, T. 2013, ApJ, 779, 134
Shimada, N., & Hoshino, M. 2000, ApJL, 543, L67
Shimizu, T., Masai, K., & Koyama, K. 2012, PASJ, 64, 24
Slane, P., Bykov, A., Ellison, D. C., Dubner, G., & Castro, D. 2015, SSRv, 188, 187
Smith, R. C. & MCELS Team 1999, in IAU Symp. 190, New Views of the Magellanic Clouds, ed. Y. H. Chu et al. (San Francisco, CA: ASP), 28
Smith, R. C., Points, S., Aguilera, C., et al. 2004, AAS Meeting, 36, 101.08
Snowden, S., Valencic, L., Perry, B., Arida, M., & Kuntz, K. D. 2004, The XMM-Newton ABC Guide: An Introduction to XMM-Newton Data Analysis
Snowden, S. L., Egger, R., Finkbeiner, D. P., Freyberg, M. J., & Plucinsky, P. P. 1998, ApJ, 493, 715
Snowden, S. L., Egger, R., Freyberg, M. J., et al. 1997, ApJ, 485, 125
Snowden, S. L., Mushotzky, R. F., Kuntz, K. D., & Davis, D. S. 2008, A&A, 478, 615
Sukhbold, T., Ertl, T., Woosley, S. E., Brown, J. M., & Janka, H.-T. 2016, ApJ, 821, 38
Sutherland, R. S., & Dopita, M. A. 1995, ApJ, 439, 365
Tang, Z., Reynolds, S. P., & Ressler, S. M. 2016, ApJS, 227, 28
Tappe, A., Rho, J., Boersma, C., & Micelotta, E. R. 2012, ApJ, 754, 132
Tappe, A., Rho, J., & Reach, W. T. 2006, ApJ, 653, 267
Tenorio-Tagle, G., Rozyczka, M., Franco, J., & Bodenheimer, P. 1991, MNRAS, 251, 318
Thielemann, F. K., Nomoto, K., Shigeyama, T., Tsujimoto, T., & Hashimoto, M. 1992, in Elements and the Cosmos, ed. M. G. Edmunds & R. Terlevich (Cambridge: Cambridge Univ. Press), 68
Tominaga, N., Umeda, H., & Nomoto, K. 2007, ApJ, 660, 516
van Dyk, D. A., Connors, A., Kashyap, V. L., & Siemiginowska, A. 2001, ApJ, 548, 224
van Marle, A. J., & Keppens, R. 2012, A&A, 547, A3
Vink, J. 2012, A&ARv, 20, 49
Vogt, F., & Dopita, M. A. 2011, Ap&SS, 331, 521
Weisskopf, M. C., Tananbaum, H. D., Van Speybroeck, L. P., & O'Dell, S. L. 2000, Proc. SPIE, 4012, 2
Welty, D. E., Lauroesch, J. T., Wong, T., & York, D. G. 2016, ApJ, 821, 118
Westerlund, B. E. 1997, The Magellanic Clouds (Cambridge: Cambridge Univ. Press)
Westerlund, B. E., & Mathewson, D. S. 1966, MNRAS, 131, 371
White, R. L., & Long, K. S. 1991, ApJ, 373, 543
Williams, B. J., Borkowski, K. J., Reynolds, S. P., et al. 2006, ApJL, 652, L33
Wilms, J., Allen, A., & McCray, R. 2000, ApJ, 542, 914
Winkler, P. F., & Petre, R. 2007, ApJ, 670, 635
Wong, T., Hughes, A., Ott, J., et al. 2011, ApJS, 197, 16
Xiao, X., & Chen, Y. 2008, AdSpR, 41, 416
Yamaguchi, H., Badenes, C., Petre, R., et al. 2014, ApJL, 785, L27
Yamaguchi, H., Ozawa, M., Koyama, K., et al. 2009, ApJL, 705, L6
Yamaguchi, H., Tanaka, T., Wik, D. R., et al. 2018, ApJL, 868, L35
Zhang, G.-Y., Slavin, J. D., Foster, A., et al. 2019, ApJ, 875, 81
Zhou, X., Miceli, M., Bocchino, F., Orlando, S., & Chen, Y. 2011, MNRAS, 415, 244
Zhu, H., Slane, P., Raymond, J., & Tian, W. W. 2019, ApJ, 882, 135